7.Praline

7.1. Introduction

The praline cream was supplied by Nestlé and was moulded into appropriate specimens for uniaxial compression loading and wire cutting. The effect of the cooling rate of molten praline on the mechanical properties of solidified praline was investigated since literature reported that there was a link between the cooling rate and mechanical properties of chocolate. The praline cream microstructure was also examined using a scanning electron microscope (SEM) in an attempt to investigate its crystalline structure.

7.2. Specimen Preparation

The praline cream was supplied as a solid block and stored in a refrigerator at 4°C to prevent microbial occurrences. The moulds for experimental testing were placed on polytetrafluoroethylene (PTFE) plates and prepared by lining the inner surface with greaseproof paper which facilitated the removal of the specimen. Depending on the test, either rectangular (cutting tests) or cylindrical (compression tests) moulds were used. To prepare the specimen, the required amount of praline was shaved off from the block using a spatula and placed in a beaker. The filled beaker was placed into a hot water bath at a temperature of 80°C and stirred continuously until the praline was completely melted. The praline cream was found to melt at 35°C, which was consistent with the most stable form VI of chocolate [5]. Overheating the praline cream caused the sugar to caramelise so it was important that the temperature of the praline cream was kept below 50°C. When the cold praline was placed in the water bath, the resulting equilibrium temperature of the molten praline was between 40-45°C. The molten praline cream was poured into the moulds and left to cool and solidify overnight. Figure 7.1 shows the molten praline in the moulds and the solidified specimens after they were cooled.

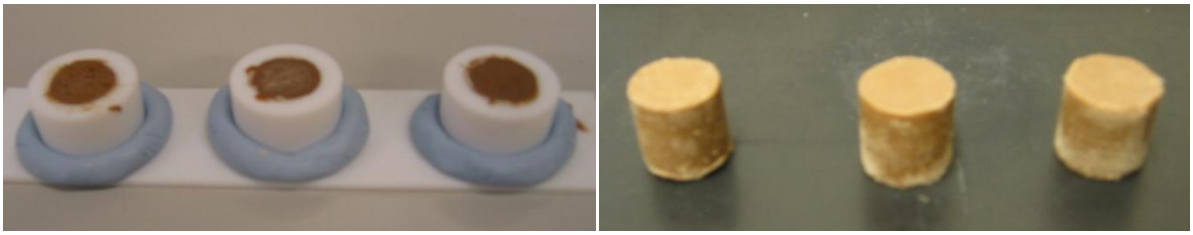

Figure 7.1 Molten praline in moulds and solidified specimens

Two methods by which to cool the praline were recommended by Nestlé. The first was slow cooling of the praline cream from its molten state to room temperature of around 19°C and the second was rapid cooling of the praline cream to sub-ambient temperature of 4°C in a refrigerator. The solidified specimens were removed from the PTFE plate by a sliding action and then carefully ejected from the mould. Specimens removed from the refrigerator would be left to warm up to room temperature of 19°C before testing. For every batch, an extra 'dummy' specimen with a thermocouple inserted into it would be used to monitor the temperature of the praline to ensure the centre of the specimen had equilibrated.

7.3. Cooling Rates Investigation

7.3.1. Effects of Cooling Rates

The effect of cooling rate on the praline cream was investigated to determine if it affected its mechanical behaviour. As mentioned in the previous section, there were two methods by which to cool the praline cream, either by cooling to room temperature referred to as "slow cooling" or sub-ambient temperature referred to as "rapid cooling". Unlike the wafer compression, the nominal stresses and strains were not used for the analysis of the praline since it was assumed that the praline underwent constant volume deformation. Instead, the true stress and true stress was plotted using the data obtained from the praline compression experiments. The true stress and true strain were calculated using Equations 7.1 and 7.2 respectively.

$$\sigma_{true} = \sigma(1 - \varepsilon) \tag{7.1}$$

$$\varepsilon_{true} = -\ln(1 - \varepsilon) \tag{7.2}$$

A batch of eight cylindrical specimens with diameter 20 mm and height 20mm was prepared, half of which were slowly cooled and the other half rapidly cooled. The specimens were then subjected to uni-axial compression testing at a constant true strain rate of 1 min^{-1} and the stress-strain curves were plotted for comparison in Figure 7.2.

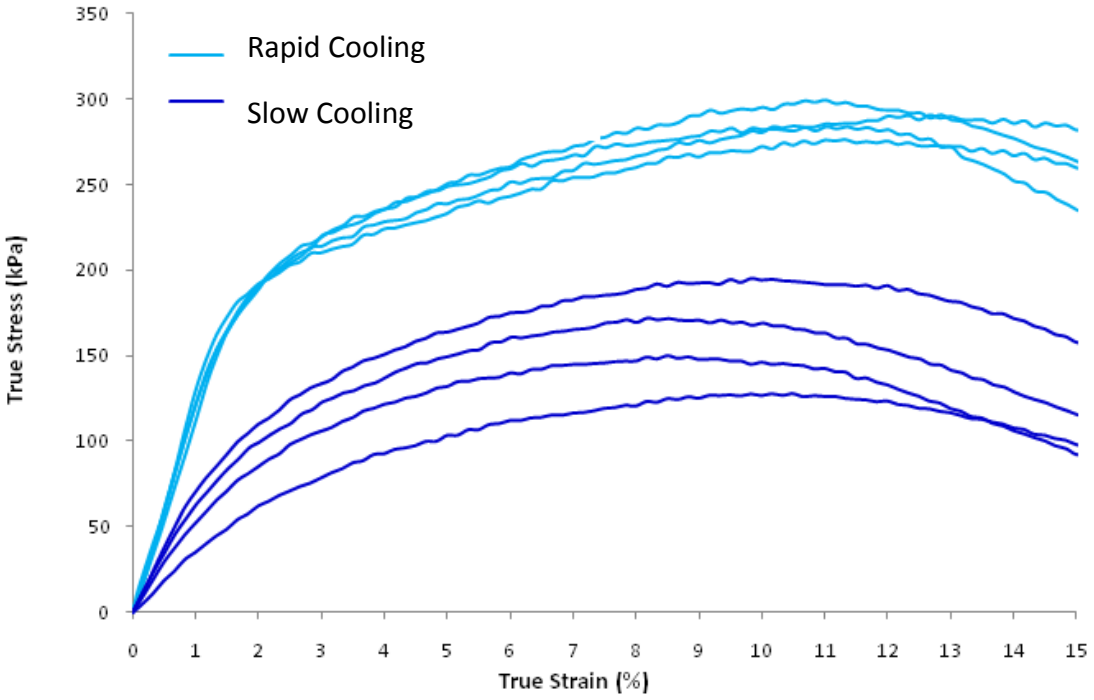

Figure 7.2 Stress-strain curves comparing specimens cooled to room and sub-ambient temperature

It was observed that slowly cooled specimens consistently deformed at lower stresses compared to rapidly cooled specimens. Rapidly cooled specimens resulted in a clear initial linear region and maximum stresses between 270-300 kPa. Conversely, slowly cooled specimens resulted in a wider scatter in stress-strain curves and hence a wider range of maximum stress from 125-195 kPa. The initial linear region was not as prominent and was less steep compared to rapidly cooled specimens, thus the praline appeared to be less stiff when slowly cooled. All future tests used specimens that were rapidly cooled to sub-ambient

temperature due to the reproducibility of stress-strain curves since the refrigerator temperature was fixed and thus allowed for better control of the cooling rate.

Investigations into the hardness of chocolate have shown that samples cooled at low temperatures were much harder than those cooled at higher temperatures [3]. Keijbets et al [116] speculated that this was because at low temperatures, smaller crystals were formed allowing for denser packing of the crystals and hence a harder chocolate. Therefore, the difference in the behaviour observed in the praline may be attributed to the size of the crystals upon cooling. Since hardness is proportional to the strength of the material, it can then be expected that rapidly cooled praline would be harder and in turn produce higher stress-strain curves.

7.3.2. Cooling Rate across the Mould

It was also important to investigate how the cooling rate varied across a mould and the corresponding effects, if any, on the mechanical properties. To do this, two cylindrical specimens of the same aspect ratio (height/diameter) of 1, but of different dimensions were prepared. The smaller specimen had dimensions Ø20x20 mm, while the larger specimen had dimensions Ø40x40 mm. Thermocouples were placed in two locations in each specimen; at the inner wall and in the centre of the mould, as shown in Figure 7.3.

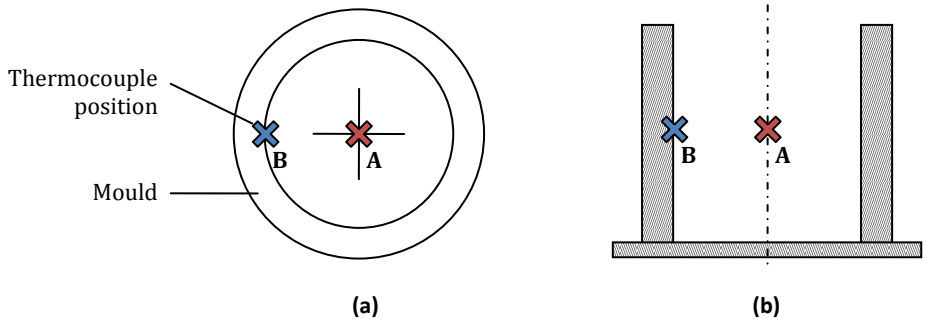

Figure 7.3 Top and cross-sectional view of the mould showing the positions of the thermocouple

The specimens were allowed to cool from the molten temperature of around 45° to a sub-ambient temperature of 4°C and temperature readings were taken at regular intervals. The experiment was performed twice for each mould size and average cooling curves were

obtained to determine if the cooling rate varied radially. The temperature at positions A and B were plotted against time for both sizes of the moulds as shown in Figure 7.4.

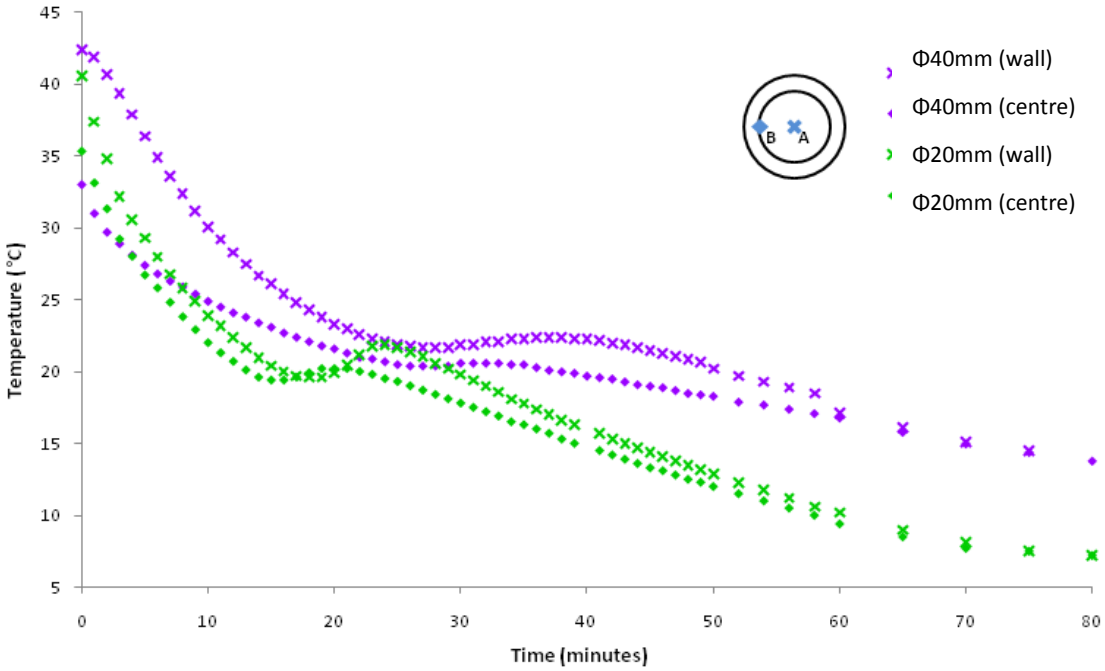

Figure 7.4 Cooling curves at two locations within moulds of sizes Ø40x40mm and Ø20x20mm

It can be seen straight away that the Ø20x20 mm specimen produced steeper cooling curves than the Ø40x40 mm specimen thus cooling faster as expected. Even at 80minutes, the Ø40x40 mm specimen was 6.7°C warmer than the Ø20x20 mm.

Considering only the Ø40x40 mm mould, the initial temperature (at time zero) at the wall was much lower at 33.0°C compared to the initial temperature in the middle of the mould which was at 42.4°C. This was reasonable since the molten praline would be expected to cool immediately upon contact with the cold wall of the mould. As the specimen cooled, it was seen that the cooling curves began closely converging after 25 minutes suggesting a uniform temperature distribution in a radial direction.

For the Ø20x20 mm mould, the difference in the temperatures at the wall (35.3°C) and in the middle (40.6°C) of the mould at time zero is less than the larger mould. However, the initial temperature at the wall and the centre for both sized moulds were similar to each other

within 2°C. The two cooling curves for the Ø20x20 mm specimen also followed each other closely after 15 minutes. There was total convergence in temperatures of both moulds at both positions after approximately 60 minutes, although the Ø40x40 mm was 7°C warmer than the Ø20x20 mm mould.

The temperatures of all the specimens eventually reached the sub-ambient temperature of 4°C, after which they were removed from the refrigerator and allowed to return to ambient temperature of 20°C before performing mechanical tests. Three specimens of each mould size were then subject to uniaxial compression testing at a constant true strain rate of 1 min^{-1} and the stress-strain curves of representative samples are shown in Figure 7.5.

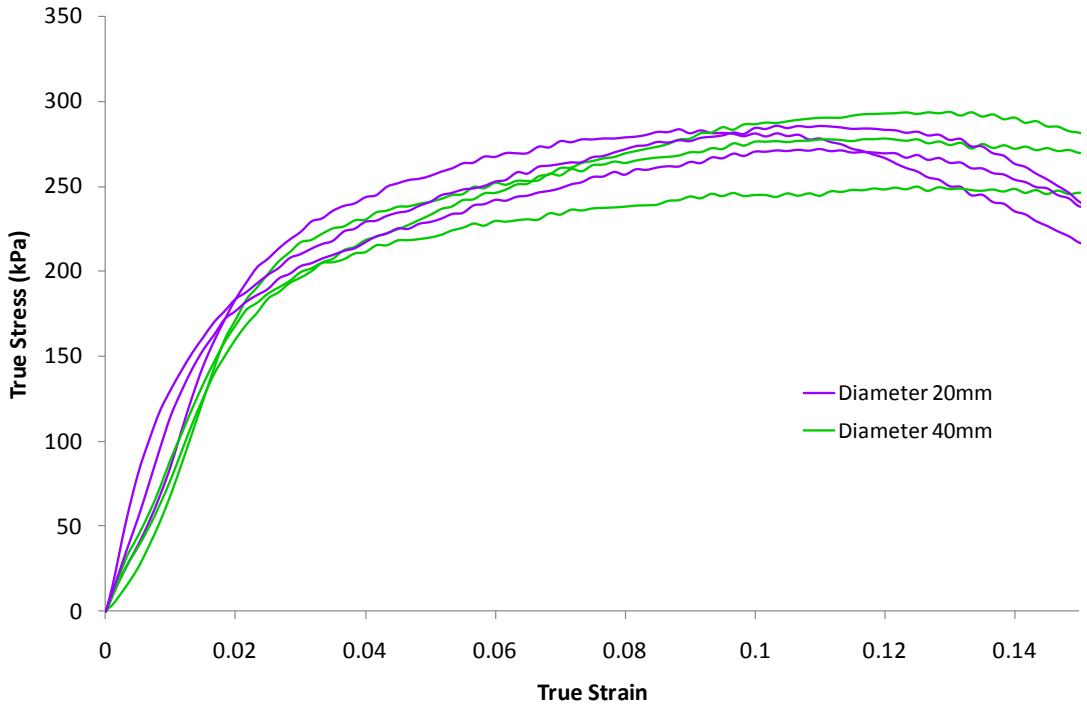

Figure 7.5 Stress-strain curves for specimens with same aspect ratio but different dimensions

Since both samples had an aspect ratio of 1, this ensured that any frictional effects between the praline and platens would be the same for both sample sizes. The results showed that the stress-strain curves were similar, suggesting that the difference in cooling rates across the mould had a negligible effect on the mechanical properties. Despite the larger

Ø40x40mm specimen displaying a slower cooling rate when compared to the Ø20x20mm mould, it was not enough to affect the deformation behaviour of the praline.

7.3.3. Cooling Rate through the Mould

The effect of the sample height on the cooling rate through the specimen was also examined. Thermocouples were inserted into the centre of specimens with the same nominal diameter of 20mm, but of heights 15, 20, 30 and 40mm. Temperature readings were taken at regular intervals while the specimens were rapidly cooled. The cooling experiment was repeated twice and an average cooling curve was obtained for each specimen height as shown in Figure 7.6.

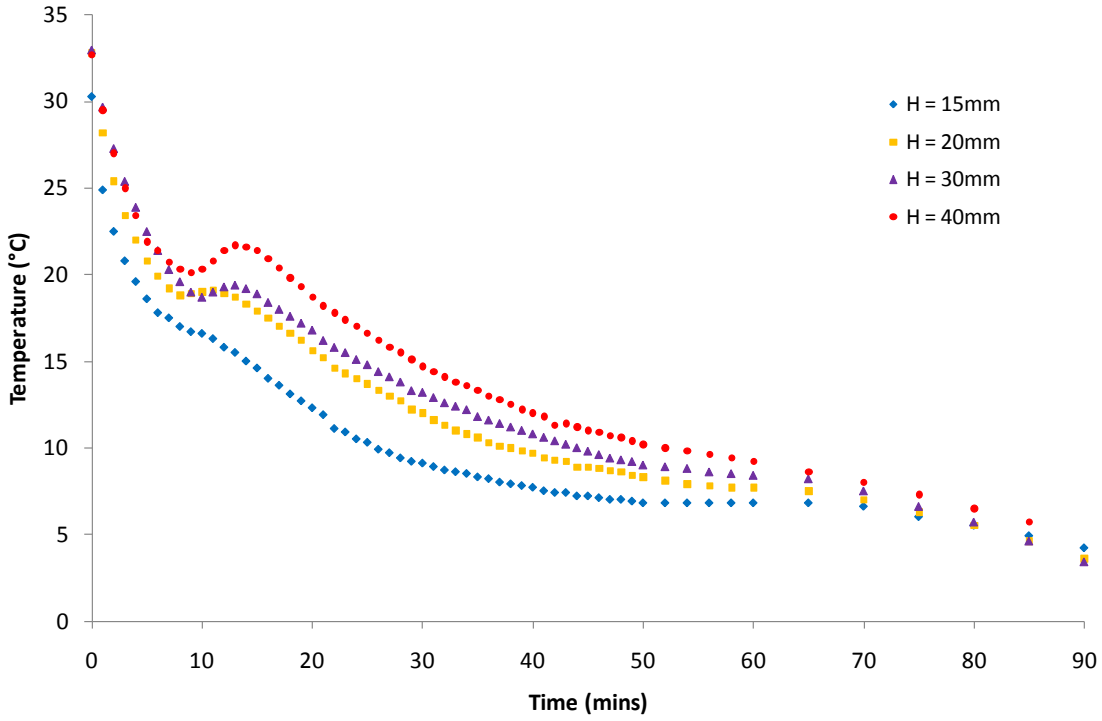

Figure 7.6 Cooling curves comparing rapidly cooled specimens of the same diameter but of different heights

It was seen that the cooling rates did not vary significantly for the specimens of heights 20 mm and 30 mm, but the 15 mm tall specimens appeared to cool more rapidly while the 40 mm tall specimen cooled at a slower rate. If it is assumed that the mould acts as an insulator and heat is conducted away from the centre of the specimen, then the majority of heat

would escape through the top and bottom of the mould. Hence it would generally be expected that shorter specimens would cool faster since a larger percentage of its surface area was exposed to the surroundings.

With reference to both Figure 7.4 and Figure 7.6, it was observed that the cooling curves plateau or in some cases form a maximum at around 20°C. This cooling behaviour has also been observed in chocolate [6] and it is attributed to the crystallisation of the cocoa butter which releases latent heat of crystallisation causing a rise in temperature in the material. This offsets the cooling rate causing the temperature curves to display a brief increase in the gradient.

The frictional effects between the loading plates and the specimen were investigated by uni-axially compressing specimens of different heights. Cylindrical specimens of the same nominal diameter of 20mm but different heights of 15, 20, 30 and 40 mm were prepared, giving aspect ratios of 0.75, 1.0, 1.5 and 2.0 respectively. For each height, eight specimens were uni-axially compressed at a constant true strain rate of 1 min^{-1} with no lubrication, and the true stress-true strain curves are plotted in Figure 7.7. The differences in the cooling rates recorded in Figure 7.6 were not expected to lead to any changes in the stress-strain response. Any differences observed in the deformation curves of the Figure 7.7 can be attributed to either friction between the platens and the specimen or the different aspect ratios of the samples.

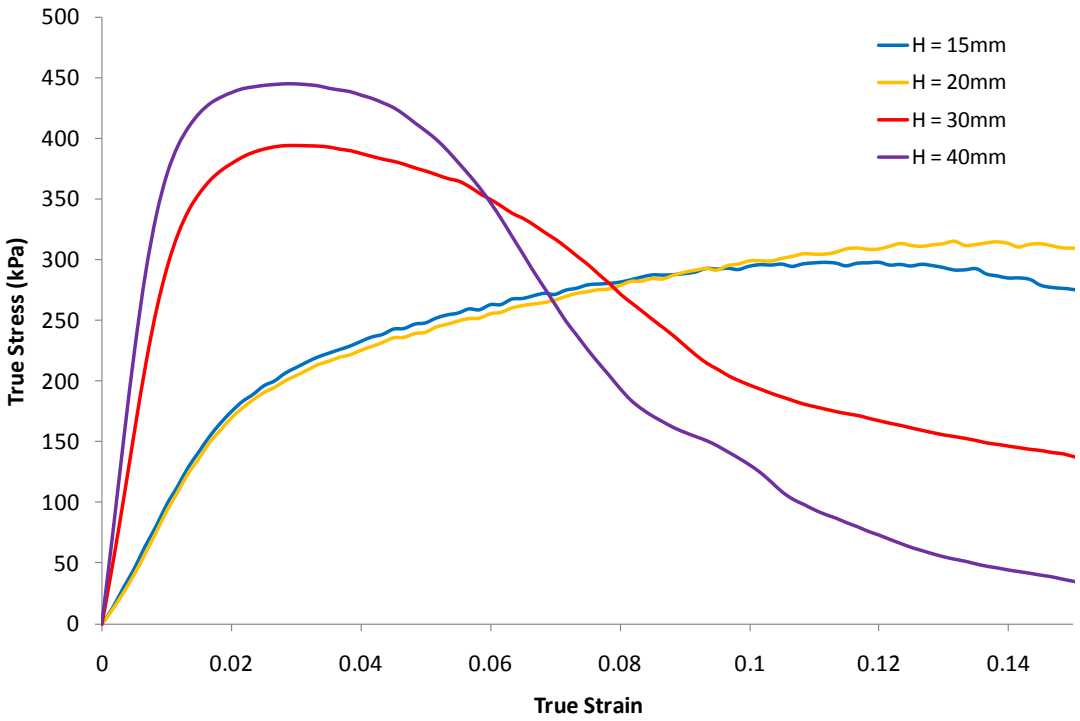

Figure 7.7 Stress-strain curves of specimens of different heights and constant diameter

The specimens of heights 15 and 20mm produced stress-strain curves that followed each other closely. By considering only the stress-strain curves of the 15 and 20mm tall specimens, it was concluded that the praline cream was self-lubricating. It was plausible that the fat content in the praline acted as a lubricant. There was no significant difference between the stress-strain curves produced and hence contact between the specimen and the loading plates can be assumed to be frictionless. As shown in Figure 7.8a, minimal barrelling was observed.

Taller specimens were expected to produce lower stress-strain curves than shorter specimens if frictional effects were significant [22]. From Figure 7.7, it can be seen that this was not the case with 30 and 40 mm tall specimens which produced stress-strain curves much higher than the two shorter specimens. Possible reasons for the trend in the data are explained below.

The taller specimens (30 and 40mm) were susceptible to a different fracture behaviour, often resulting in the specimen 'splitting' near either the top or bottom (Figure 7.8c), or a

'mushrooming effect' would occur where the praline cream would appear to gather at the bottom in a manner observed in Figure 7.8b.

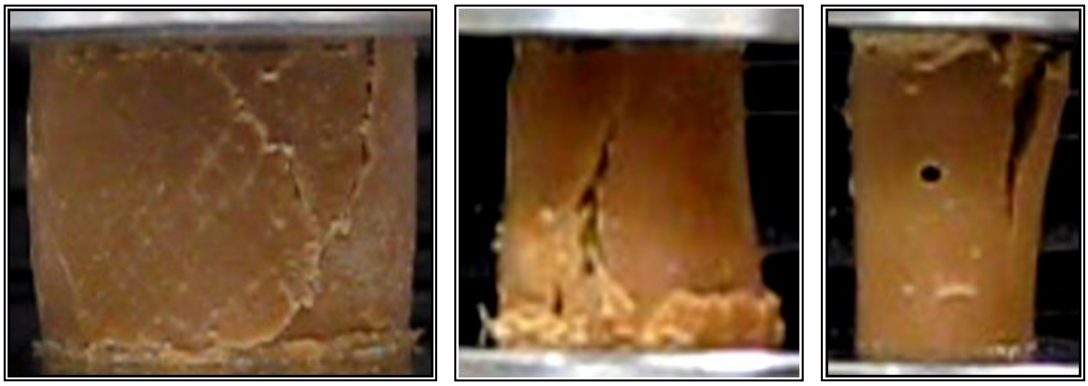

Figure 7.8 Praline deformation of height a) 20mm, b) 30mm, c) 40mm

The 'mushrooming' effect where the praline was seen to 'bunch' at the bottom of the specimen (Figure 7.8b) may indicate the praline is being squashed, requiring a higher stress is to overcome the resistance from the praline being gathered at the bottom. It is apparent that the taller specimens (Figure 7.8b & c) undergo a different mode of fracture than the shorter ones (Figure 7.8a), requiring more energy and hence a higher stress is observed. It has been suggested that cracks that develop to split the specimen were known to occur in compression testing when the ends of the specimen had negligible friction [117].

It was observed in specimens of heights 15mm and 20mm, that cracks initially propagated through the material at approximately an angle of 45° to the line of loading and a diagonal lattice pattern was formed on the surface. The larger cracks would meet and a single crack would travel roughly along the line of loading, forming a Y-shape, as can be seen in Figure 7.8a. While this behaviour indicates shear failure, it has been suggested that for quasi-brittle materials the microscopic fracture mechanisms are not that of shear failure. Bažant and Xiang [117] have reported that shear slip is not possible in quasi-brittle materials such as concrete or ceramics because cracks that are inclined to the direction of the compressive load have rough surfaces which interlock preventing slip. It is believed instead that there are

three mechanisms that lead to failure under compression: a) Cracks around pores, b) Cracks around particles in composites, c) “Wing-tip” microcracks

As shown in Figure 7.9, the cracks grow from pores existing within the specimen in the direction of the compressive load. Cracks can develop around particles in composites e.g. rigid fibres, either above and below the particle (see Figure 7.9b) or in between particles (see Figure 7.9c). These cracks develop from weak interfaces between the crystal structure at an angle to the compressive load. Slip causes cracks to grow as shown in Figure 7.9d, where they curve towards the axis of loading.

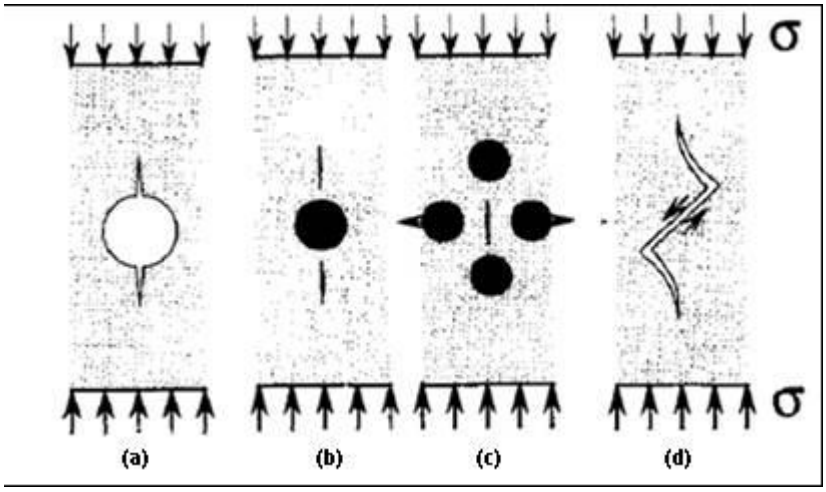

Figure 7.9 Failure mechanisms under compression [117]

In solid form, the praline cream has a crumbly texture and appears to be brittle and it is possible that the above compressive failure mechanisms occur within the praline specimen as it is compressed. The wafer crumbs within the praline may also act as inclusions promoting the second failure mechanism (Figure 7.9b) mentioned above. However it was not possible to determine the exact microscopic physical mechanisms occurring as the praline was compressed, and so it was decided to examine the microstructure of the praline under the SEM.

The deformation mechanisms, such as mushrooming and splitting, observed in the specimens with larger aspect ratios made them unsuitable for analysis. The results obtained

for the 30 and 40mm tall specimens were not considered and all future compression experiments were carried out using specimens with dimensions of Ø20x20mm.

7.4. Uniaxial Compression Testing

7.4.1. Rate Dependency

The specimens prepared for the compression tests were cylindrical with dimensions of Ø20x20mm and cooled to sub-ambient temperature of 4°C before being allowed to equilibrate to an ambient temperature of 20°C. Initially, specimens were tested at constant speeds of 1, 5 and 10 mm/min and Figure 7.10 gives the deformation curves of three specimens compressed at each of these speeds. It was observed that the gradient of the linear elastic region of the stress-strain curves varied with speed indicating that the praline cream could potentially be a rate dependent material. To ensure that that the mechanical behaviour could be characterised accurately, the praline cream was tested under constant true strain rate conditions.

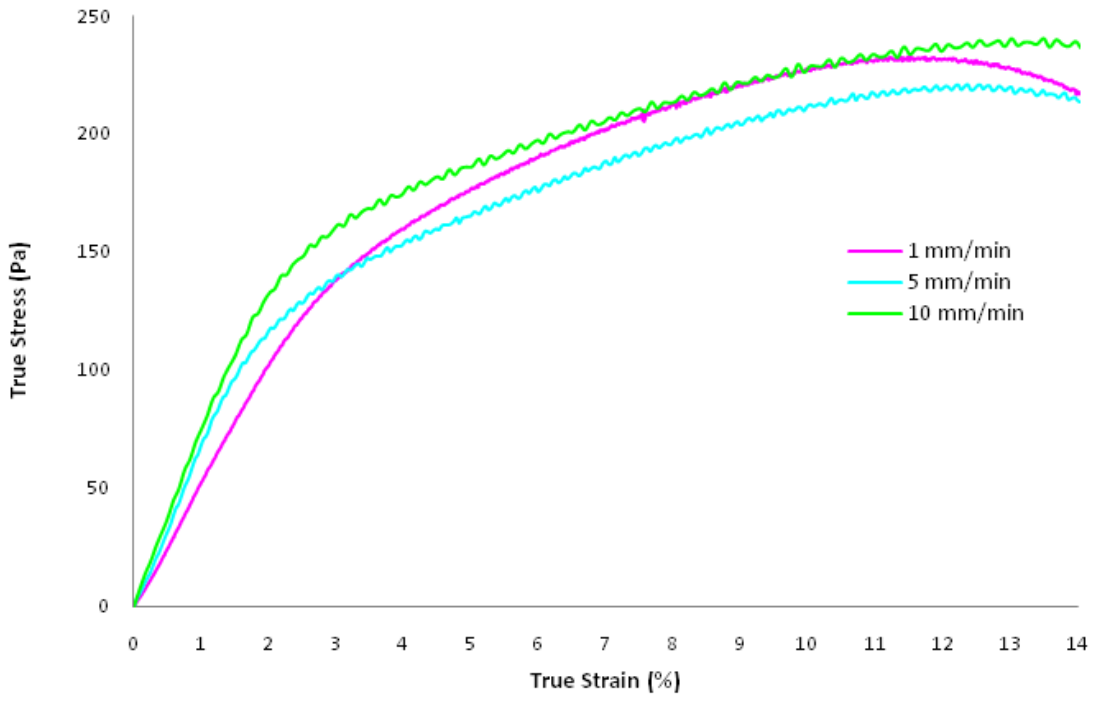

Figure 7.10 Stress-strain curves for Ø20x20mm specimens tested at constant speeds

Eight specimens were tested at each of the constant true strain rates of 0.1, 1 and 10 min^{-1} and representative true stress-true strain curves were plotted in Figure 7.11. It can be seen that there is no significant effect of the strain rate on the elastic region of the curves.

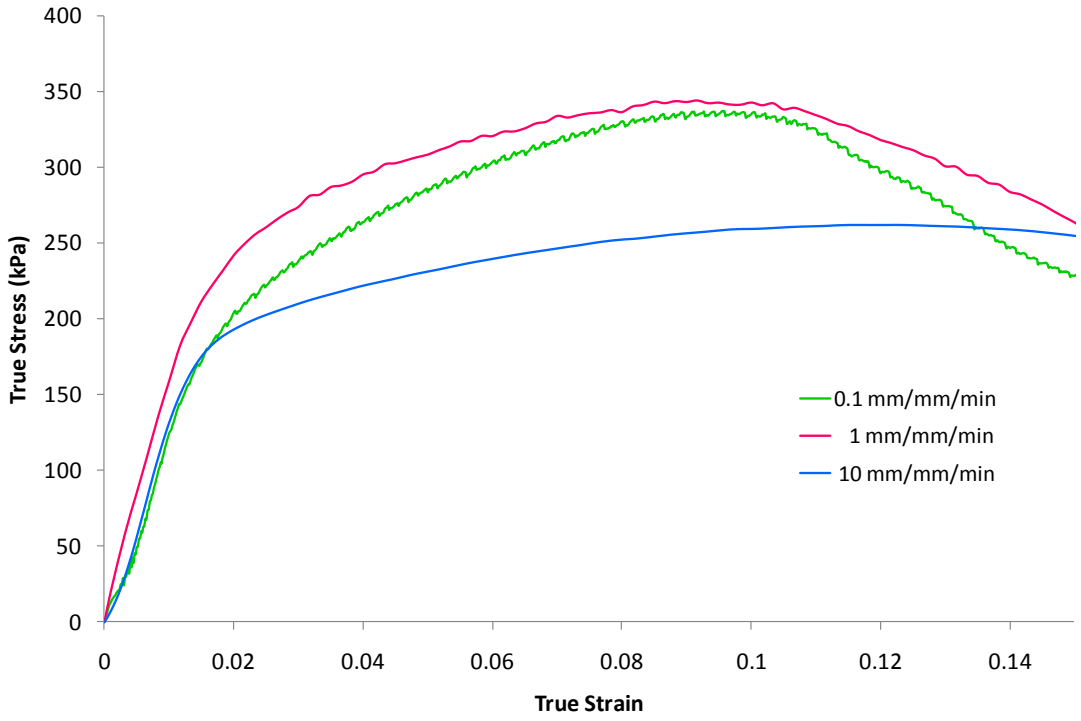

Figure 7.11 Stress-strain curves for specimens Ø20x20mm compressed at different strain rates

For all tests, an initial linear (elastic) region on the stress-strain curves was observed, followed by a non-linear (plastic) regime. It was also observed that cracks would first appear in the material at the point of maximum stress i.e. the point of fracture. Beyond this point the stress declined rapidly as the material was permanently damaged by the compressive force. Figure 7.12 shows the various stages of the deformation of a praline sample compressed at 1 min^{-1} before any fracture has occurred.

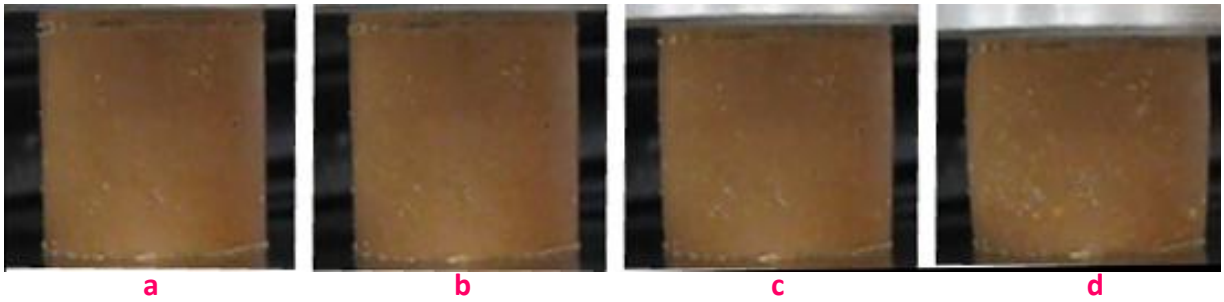

Figure 7.12 Different stages of the deformation of a praline sample compressed at a true strain rate of 1 min^{-1} a) ε=0.01, b) ε=0.02, c) ε=0.07, d) ε=0.12

From the stress-strain curves obtained from compression testing, there were two points of interest: the point at which the linear regime ended and the maximum stress at which fracture occurs. The linear regime is indicative of an elastic region, from which the elastic modulus (*E*) can be obtained from the slope of the graph.

The point where the linear region ends is known as the proportionality limit (σ_{PL}) and in cases where the transition from linear to non-linear on the stress-strain curve is clearly defined, it is often taken to be the yield strength, (σ_Y) [118]. For the data obtained from compression tests performed on the praline cream, the linear region is fairly visible and hence σ_{PL} has been found and taken to be σ_Y. The maximum stress on a stress-strain curve is defined as the fracture stress, σ_F, of the praline cream since it was at this point where cracks were first observed. The results for each strain rate are summarised in Figure 7.13.

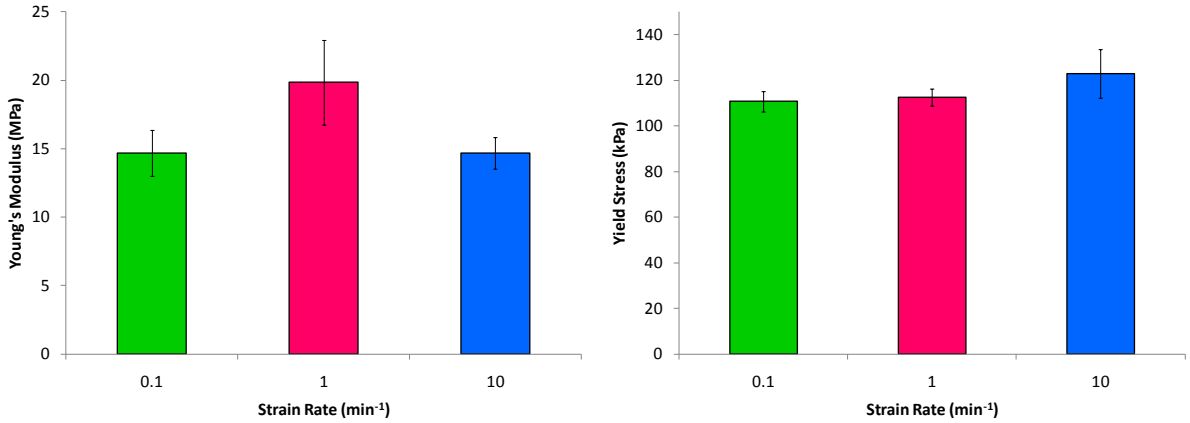

Figure 7.13 The a) Young's Modulus and b) Yield stress at different strain rates

Furthermore, single averaged values for σ_Y, σ_F and E were calculated to be 115 ± 6 kPa, 295 ± 13 kPa and 16.4 ± 1.9 MPa respectively, by assuming the praline was independent of strain rate, as suggested by the results obtained.

7.4.2. Loading and Unloading

The specimens were moulded into cylinders with dimensions Ø20x20 mm. They were uni-axially compressed at a constant true strain rate of 1 min^{-1} to a fixed crosshead displacement of 0.3 mm (ε=0.015) before being unloaded. Greaseproof paper was used to line the top and bottom loading plates in order to prevent the praline cream from sticking to either surface when unloaded. Figure 7.14 shows a sample loading-unloading curve obtained.

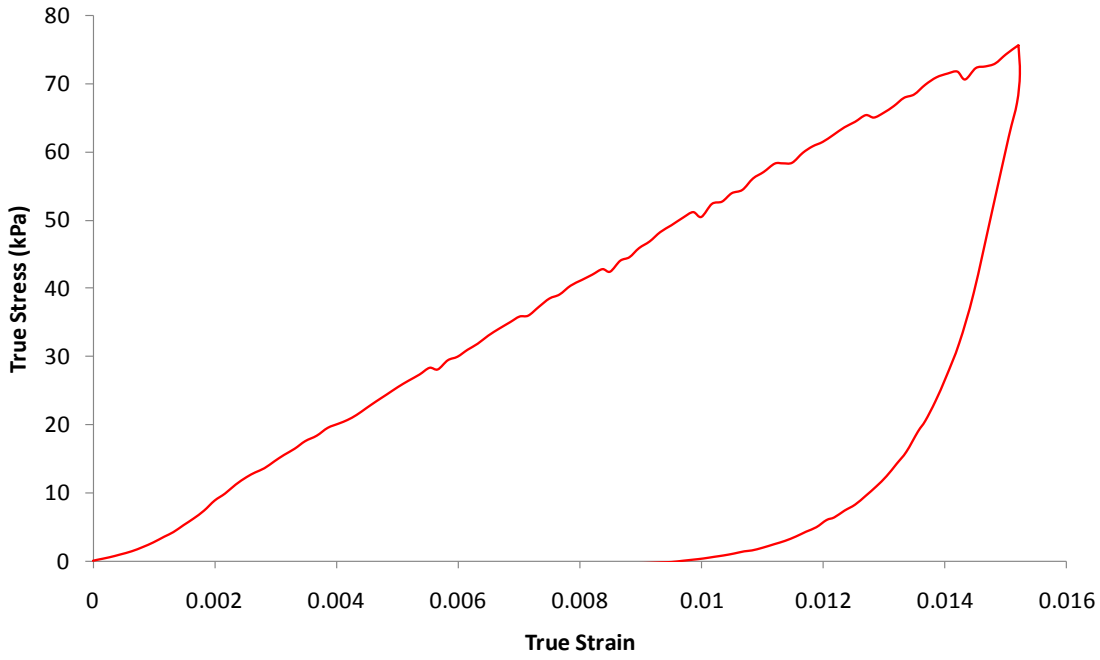

Figure 7.14 Loading and unloading curve for a specimen compressed at constant true strain rate

It was observed that the praline cream exhibited plastic deformation since the unloading curve did not return to the origin nor did it unload with the same gradient as which it was loaded.

7.5. Cutting Tests

Specimens were moulded into rectangular blocks of dimensions 20 x 20 x 30mm. Due to the soft nature of the praline it was not possible to clamp the specimen such that the blade would be able to leave the specimen through the bottom. Instead, the specimen was placed on the loading plate and the blade was lowered into the specimen (Figure 7.15) to a crosshead displacement of 18 mm. Displacement was not specified to the entire height of the specimen (20 mm) to avoid damaging the test rig and the Instron load cell.

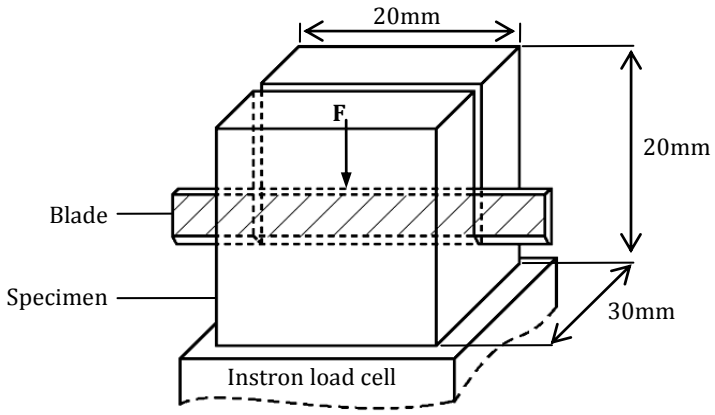

Figure 7.15 Schematic of the setup used for the cutting of the praline

As with the wafer cutting tests, both the sharp and blunt edges of the blade were used to perform the cutting tests. The load-displacement profiles produced by each edge of the blade are shown in Figure 7.16. Naturally, the sharp edge exerted less force than the blunt edge but in both cases a steady state force was not observed. A crack tended to propagate prematurely ahead of the blade and fast fracture occurred shortly after the blade had entered the material. The blade cutting produced no useful data to determine fracture properties, so further cutting experiments focussed on using wires instead of blades.

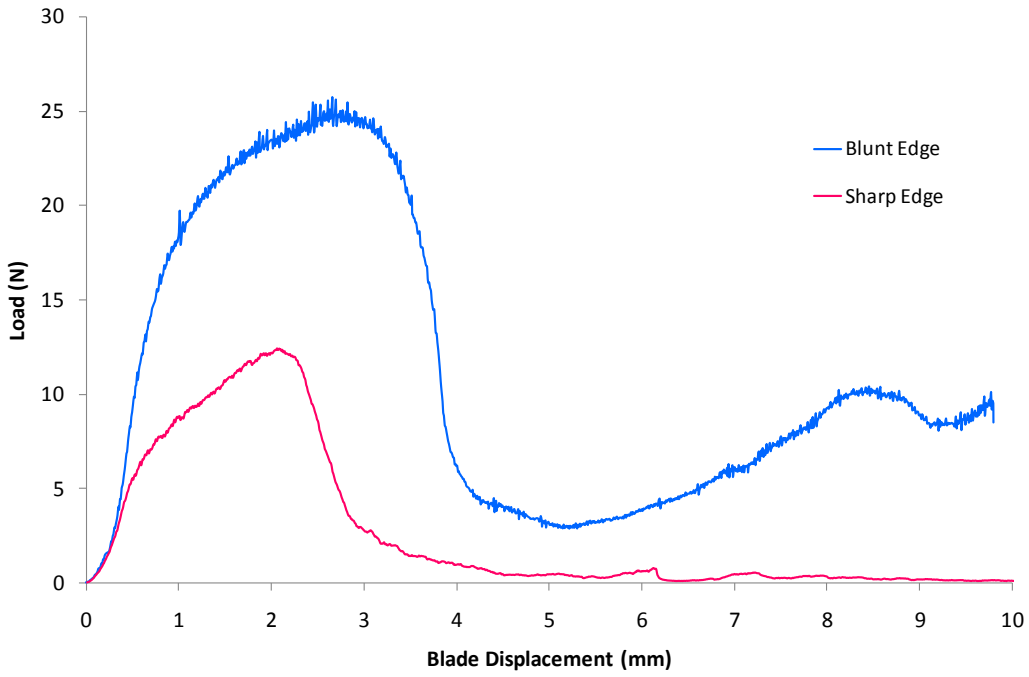

Figure 7.16 The load-displacement output using the sharp and blunt edges of the blade

The wire cutting proved to be more successful in obtaining a steady state force and thus fracture data. Figure 7.17 shows a load-displacement graph obtained from a single specimen cut at a speed of 5 mm/min with a wire diameter of 0.3 mm and accompanying photos to demonstrate the behaviour observed at different stages of the deformation.

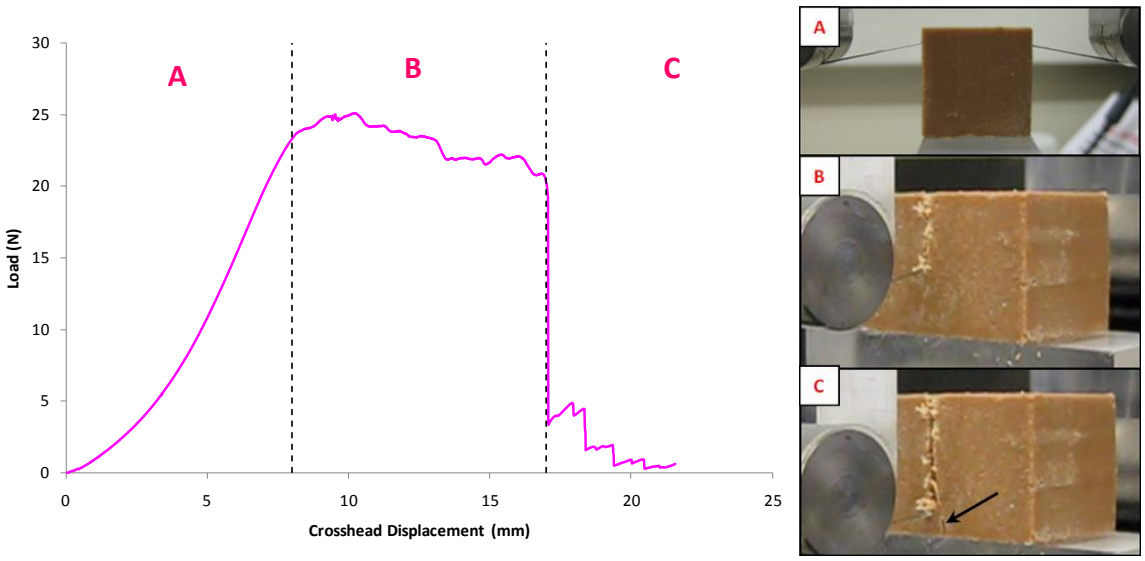

Figure 7.17 Load-displacement graph of wire cutting with images at the different stages

As the wire entered the praline, it was observed to bow upwards as shown in photo A, this was accompanied by a ramped increase in the force (region A). The force then stabilised (region B) as cutting reached a steady state and a maximum load known as the cutting force, F_c. At the end of this region, there was an immediate drop in the force which was observed to occur when a crack propagated ahead of the wire, as indicated in photo C by an arrow. In the majority of the tests, the crack formed at an angle away from the line of cutting, and although the force dropped, it did not go to zero straight away and instead 'staggered' as in region C of Figure 7.17, as the wire was still in contact with the praline material around it.

Tests were carried out at a range of speeds and it was found that the praline produced values of maximum load that appeared to be independent of speed (Figure 7.18). This was found to be true for all wire diameters used, and as expected it was found that the maximum force achieved increased with wire diameter. Figure 7.19 shows three specimens tested at a cutting speed of 5 mm/min for wire diameters of 0.3, 0.4 and 0.6 mm to illustrate this.

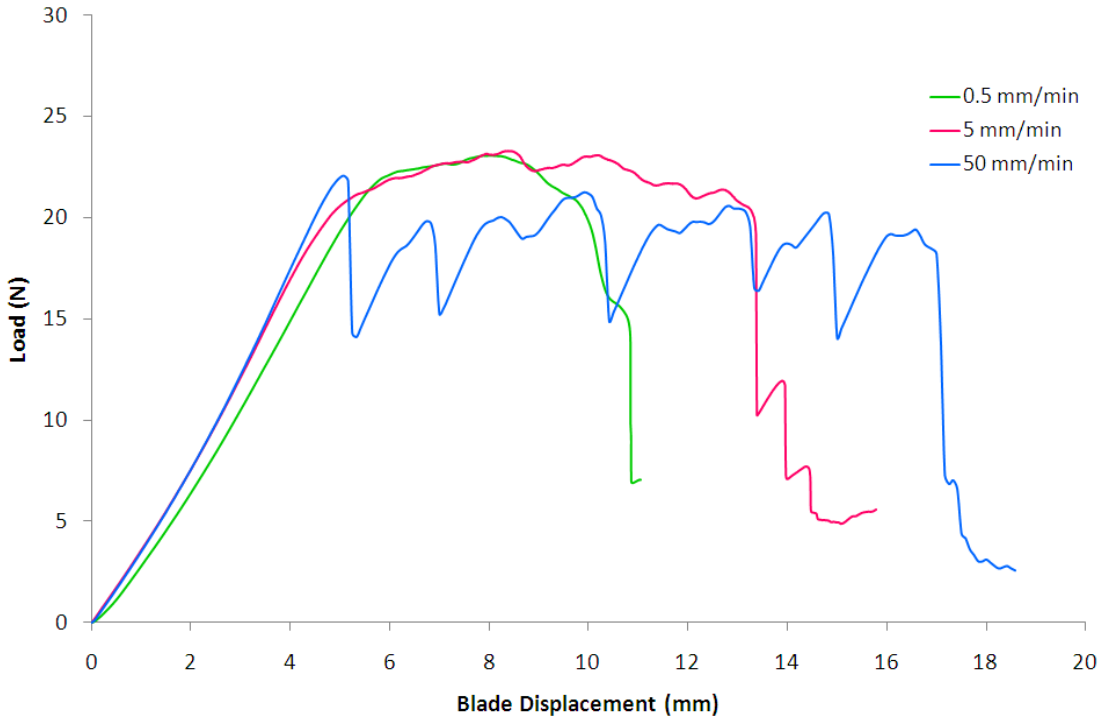

Figure 7.18 Comparison of cutting forces at different cutting speeds for a wire diameter of 0.3mm

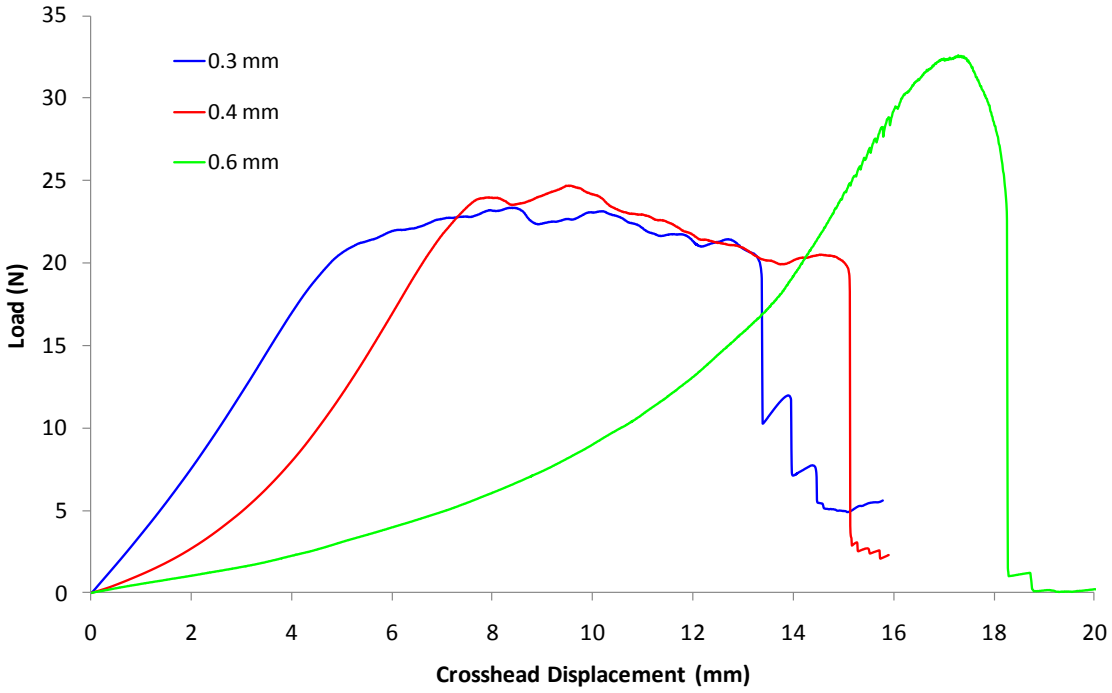

Figure 7.19 Comparison of cutting forces for different wire diameters at a cutting speed of 5mm/min

The graphs obtained for the wire diameters 0.3 and 0.4 mm showed clear steady-state cutting regimes. However, for the wire diameter 0.6 mm, this was not the case and the graphs obtained showed a rounded peak rather than a plateau. However there was consistency in that the maximum force achieved fell within the range of 28-32 N.

The data obtained from the wire cutting was used to determine values for fracture energy, G_C using Equation 7.3 [39, 40, 96] which assumes a linear relationship between the wire diameter, d, and the cutting force, F_c.

$$\frac{F_c}{B} = G_C + (1+\mu)\sigma_Y d \qquad (7.3)$$

The yield stress (σ_Y), coefficient of friction (μ) and specimen width (B) are the other parameters required in Equation 7.3. The fracture energy is determined graphically by plotting F_c/B against d for different cutting speeds as shown in Figure 7.20.

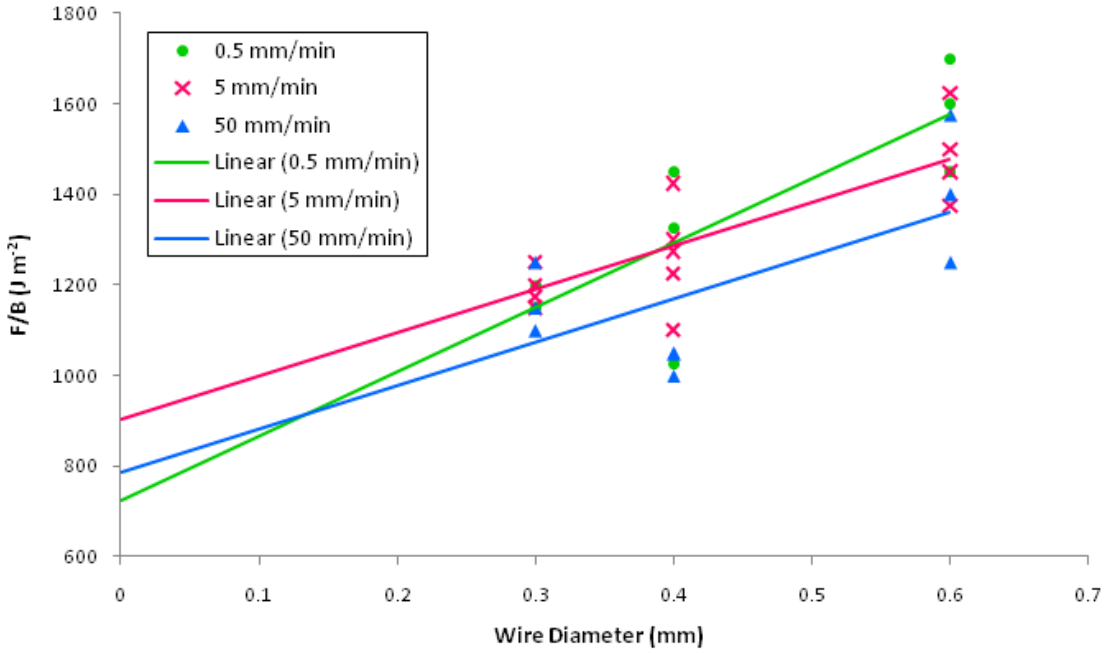

Figure 7.20 Graph showing the relationship between steady state cutting force and wire diameter

The data points in Figure 7.20 are fitted with a linear line of best fit for each cutting speed. The lines are extrapolated to the y-axis and the intercept value represents the fracture energy (G_C). The term $(1 + \mu)\sigma_Y$ can also be obtained from the gradients. The values obtained for the gradient of the slopes are not as expected. If σ_Y is taken to be 115 kPa (as calculated from the compression tests in Section 7.4.1), the coefficient of friction values are found to be extremely high ranging between 7-10 for all three cutting speeds. On the other hand, if the coefficient of friction is assumed to be approximately zero (in an ideal frictionless situation), the value for σ_Y is still up to around 10 times larger than the value found from the compression tests. The fracture energy and yield stress values (assuming no friction) are summarised in Figure 7.21.

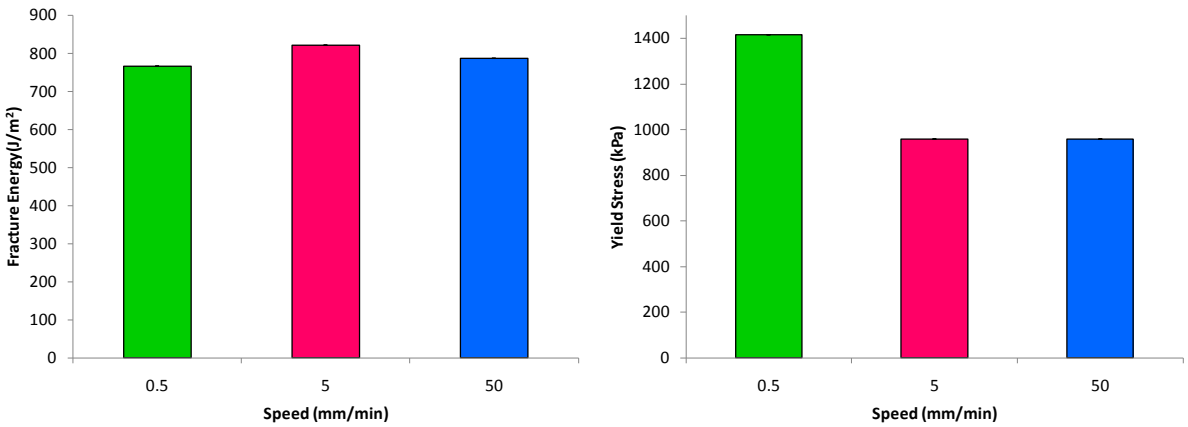

Figure 7.21 The a) Fracture energy and b) Yield stress assuming frictionless conditions for samples tested at different speeds

The wire cutting results with different diameters showed that a steady state force was unattainable for the largest size wire, which in this case was 0.6 mm. There was a large discrepancy between the yield stress obtained from the wire cutting and uniaxial compression. The wire cutting tests required using smaller diameter wires in order to attempt to increase the accuracy of the results. The fracture energy calculated for the praline was also compared to other soft solid foods such as Gouda cheese which had a fracture energy of 10 J/m^2[21, 22]. While this value was lower than the praline value, it also possessed a much lower yield stress as well. The fracture energy of another soft solid, gelatine ranged between 1-6 J/m^2 [39, 40] while the fracture energy of foods such as carrots and apples were as high as 200 J/m^2 [119].

7.6. Microscopy

The praline cream was examined using the cryo-stage of the Scanning Electron Microscope (SEM). Figure 7.22 shows images obtained from 400 and 700x magnification that can be compared to a cryo-SEM image of dark chocolate obtained from literature [120].

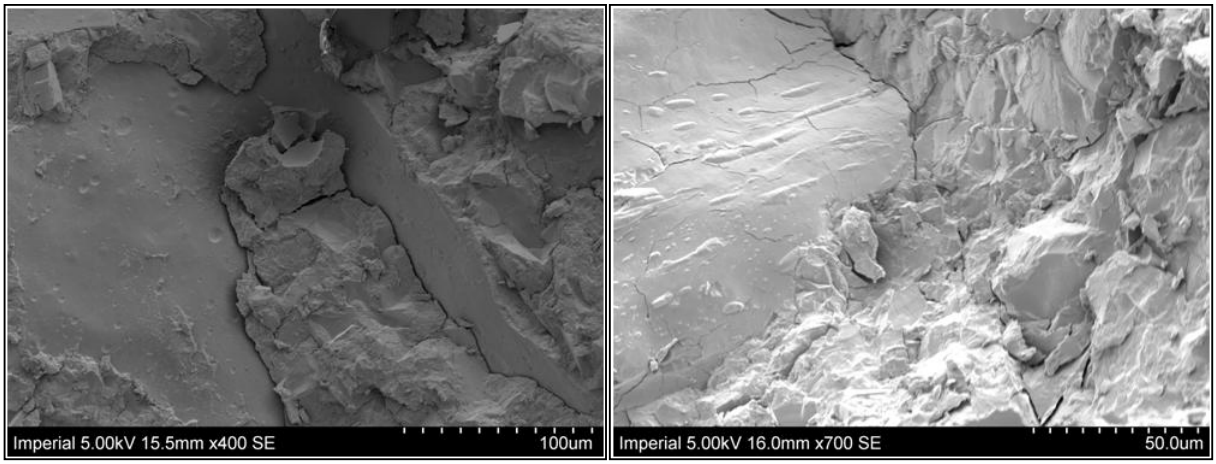

(a) **(b)**

Figure 7.22 Micrographs of the praline at different levels of magnification

James and Smith imaged the surface of bloomed and unbloomed chocolate under a cryo SEM and observed that it was only in the bloomed condition where the fat crystals are visible, emerging from the chocolate since they are pushed to the surface [120]. The images in Figure 7.22 can therefore be assumed to be images of the surface of the praline cream with no information about the crystalline structure.

7.7. Summary

The cooling rate was shown not to affect the compressive deformation response of the praline, however the temperature to which the molten praline was cooled did affect the mechanical response. The samples which were allowed to solidify at a sub-ambient temperature were stiffer and had a higher yield stress which was consistent with chocolate in which lower temperatures resulted in smaller densely packed crystals. Further uni-axial compression tests suggested that the praline was self-lubricating and a rate-independent material. The deformation of the praline was initially linear elastic with a Young's modulus of 16.4 MPa followed by a plastic region with a yield stress of 0.115 MPa and maximum stress of 0.295 MPa at which point fracture of the solid praline samples occurred. Wire cutting experiments were performed on praline samples at a range of cutting speeds and using different sized wire diameters. The microstructure of the praline was observed under the SEM using the cryo-stage but no crystal structure could be seen.

8.Conclusions

8.1. Mechanical testing

Uni-axial compression tests were performed on stacks of circular wafer sheets. The stress-strain curves indicated that the wafer was a brittle foam. From the stress-strain curves, the gradient of the elastic region was calculated to find the apparent compressive modulus of the wafer and the stress at the end of this region was measured to obtain the fracture stress. The results showed that the deformation was independent of the orientation of the reedings between adjacent wafer sheets. The compression speed had no noticeable effect on the deformation indicating that the wafer was a rate independent material. The compressive modulus and pattern of the plateau region was dependent on the number of wafer sheets in the stack, while the fracture stress was independent of the stack size. This supposed increase in modulus with wafer stack height was due to the progressive failure of individual wafer sheets in the stack. A single wafer sheet was compressed and the compressive modulus was found to be 1.32 MPa with a fracture stress of 0.34 MPa. Smaller square wafer sheets were compressed to determine the representative volume element of the wafer necessary for in-situ SEM and XMT testing, as well as finite element modelling. The RVE was determined to be 2.5x2.5 mm which included one reeding in each direction.

Three point bending of wafer sheet beam specimens were tested using different dimensions and at different speeds. As with the compression, the wafer sheet deformation in bending was independent of speed. The apparent flexural modulus was estimated from the load-deflection data and by assuming that the height of the beam was the maximum distance between the top and bottom reedings of the wafer. The maximum flexural modulus was calculated to be 959 MPa which was three orders of magnitude larger than the compressive modulus. The large discrepancy between the two values indicated that the wafer was a sandwich structure with two stiff outer skins and a weaker core.

Cutting experiments were performed on square wafer sheet specimens to determine how the relative position of the reeding and the blade influence the fracture of the wafer. When the sharp edge of the blade penetrated the wafer along a reeding, the crack propagated ahead of the blade tip along the reeding, splitting the specimen into two parts. When the blunt edge of the blade was used, there was no crack propagation ahead of the blade regardless of whether the wafer was cut along a reeding or between two reedings. However, the load-displacement profile was dependent on the position of the blade within the wafer. The wafer was also tested using wire-cutting which produced a sawtooth load-displacement profile with no fracture propagation ahead of the wire. Since the crack path of the wafer could be controlled, this method of cutting shows great potential to be applied in the future.

8.2. Microstructure

The bulk density of the wafer was measured using a solid displacement technique with glass beads while the solid density was measured using the helium gas pycnometry method. By combining the results from the two density values, the relative density of the wafer was calculated to be 0.286. This value was within the accepted range (0.05-0.3) of relative densities for foams.

Optical light microscopy was used to observe the cross-section of the wafer. The images showed that the centre of the wafer was cellular in nature and designated as the core. The outer layers were designated as the skins and considerably more dense than the core. The skin thickness, core thickness and reeding-to-reeding distance were measured from the optical micrographs to characterise the wafer dimensions.

Scanning electron microscopy produced higher quality images than the optical microscope. The porous core and the dense skins were more easily identifiable and it could be seen that the skin layer followed the contour of wafer shape. Thus the skin was of a constant thickness while the core thickness was variable with a maximum value at the reedings. The core possessed large closed cell pores with thin cell walls and some degree of interconnectivity. The skins were dense but also possessed small closed cell pores. The images of the wafer surface showed that it was contoured and covered with micropores. Some of the reedings

were also seen to have large longitudinal pores formed due to the removal of the wafer sheet from the baking plates.

X-ray microtomography was used to scan an RVE of the wafer. The images slices produced were used to reconstruct a three dimensional volume of the wafer. The resolution of the XMT scan was fine enough (5μm per voxel) to identify the pores in the skin as well as most of the thin cell walls of the core. Using imaging software, the porosity of the entire wafer was determined to be 0.765. The virtual wafer was discretised into the skin and core regions which each possessed porosities of 0.6 and 0.85 respectively. This proved quantitatively that the core was a cellular foam while the skins were closer to solid structures with pores. Another advantage of X-ray tomography was that it was possible to use the 3D volume to generate a meshed grid with which to perform a finite element analysis.

The Microtest rig module provided the capability of in-situ testing within the SEM which allowed the deformation to be observed in real time while producing a synchronised load-displacement curve. In compression, cracks first formed and propagated along the cell walls of the core while the skins remained relatively intact. The core was crushed throughout the plateau region of the deformation curve with some parts of the skin also showing signs of damage. During the densification stage, the core was fully crushed and the wafer was almost fully compacted. Compression of the wafer stack confirmed the progressive fracture of the individual wafer sheets and accounted for the large peaks in the plateau region of the deformation curve. In-situ bending tests showed that the initial fracture occurred in the bottom wafer skin and rapidly propagated through the core to the top skin. These in-situ experiments visually confirmed that the wafer core was dominant in compression while the skins were dominant in flexure. Blade cutting tests showed spalling of the wafer, with the crack favouring the reedings as well as the larger pores observed on the wafer skin. For specimens cut along the reeding, cracks initially followed the reeding before propagating across reedings perpendicular to the cutting direction. When the wafer was cut between reedings, the crack propagated across the wafer towards a reeding before eventually spalling.

A static in-situ XMT test was performed on a wafer sample and compressed until the wafer fractured. The reconstructed scans showed qualitatively that the core fractured throughout the sample while the skins remained intact.

8.3. Analytical Calculations

The analytical model divided the wafer into skin and core partitions with dimensions obtained from microscopy. The wafer was analysed as a sandwich beam in bending and as a two layered composite in compression. A modified version of Timosheko's beam theory was implemented which accounted for the shape of the reedings in the wafer geometry. The calculated elastic modulus of the skin and core was found to be 1710 MPa and 1.00 MPa respectively. The results quantitatively showed that the skins were considerably stiffer than the core.

The cellular microstructure of the wafer was analysed using numerous equations for foams in order to calculate the compressive modulus and fracture stress of the solid wafer material. The Gibson & Ashby equation which is the most widely used in literature predicted a solid modulus of 61.5 MPa and fracture stress of 13 MPa. The in-situ compression tests showed that the core accounted for the brittle foam behaviour of the wafer and the image analysis of the reconstructed wafer volume found that the porosity of the core conformed to that of a foam. Using the relative density of the core, the Gibson & Ashby equations predicted a solid modulus of 200 MPa and fracture stress of 31 MPa.

8.4. Numerical Modelling

A finite element analysis was conducted on an idealised repetitive geometry of the wafer based on the dimension obtained from optical micrography. The model was partitioned into the skin and core regions, each assigned with the respective modulus values calculated analytically. The crushable foam material model was applied to the core so that the deformation beyond the elastic stage could be modelled. In compression, the model slightly overpredicted the apparent modulus while in bending the model under predicted the stiffness when compared to the experimental data.

The 3D volume of the wafer reconstructed from the XMT scan was used to generate a tetrahedral meshed grid suitable for finite element analysis. This allowed the actual architecture of the wafer to be modelled with a simple linear elastic material model applied to the elements of the solid wafer. An inverse analysis was performed to determine the solid modulus which corresponded to an apparent modulus equal to the value obtained experimentally. This value was found to be between 150-200 MPa which was quite similar to the value of 200 MPa which was calculated analytically using the relative density of the core. The fracture of the wafer beyond the elastic region was simulated by implementing a damage criterion with element deletion. After investigating numerous damage models within the Abaqus material library, the 'ductile damage for metals' material model was selected. The damage was initiated by a plastic strain criterion and the damage evolution was governed by a fracture energy. These two parameters were reduced to minimal numerical values so that the damage material model would behave in a brittle manner. Hence the yield stress input parameter corresponded to the fracture stress of the cell wall material and initiated the element deletion. An inverse analysis to determine this fracture stress led to values between 25-50 MPa which compared quite well to the value of 31 MPa which was calculated analytically.

The FE output deformation curve possessed an initial linear region followed by a jagged plateau. The deformation plot from the FE analysis was compared to the experimental stress-strain curves and shown to have quite similar trends. The brittle collapse stress was slightly underpredicted by the FE model, but the plateau region matched the experimental data quite well. Visually, it could be seen that the maximum stresses initially developed within the core region and followed by element deletion. As the model was further compressed, the broken cell walls of the core interacted with each other due to the contact implemented between elements. The deformation predicted by the FE model was observed experimentally from the in-situ SEM and XMT compression tests. The finite element model predicted the response of the wafer in compression to a high level of accuracy both qualitatively and quantitatively.

8.5. Praline

The praline was provided as a solid block and thus needed to be melted in order to produce specimens for testing. The effect of the cooling rate on the mechanical properties of the solid praline was investigated by performing uni-axial compression experiments on cylindrical samples. The cooling rate was shown not to affect the deformation response of the praline, however the temperature to which the molten praline was cooled did affect the mechanical response. The samples which were allowed to solidify at a sub-ambient temperature were stiffer and had a higher yield stress which was consistent with chocolate in which lower temperatures resulted in smaller densely packed crystals. Further uni-axial compression tests suggested that the praline was self-lubricating and a rate-independent material. The deformation of the praline was initially linear elastic with a Young's modulus of 16.4 MPa followed by a plastic region with a yield stress of 0.115 MPa and maximum stress of 0.295 MPa at which point fracture of the solid praline samples occurred. Wire cutting experiments were performed on praline samples at a range of cutting speeds and using different sized wire diameters. The microstructure of the praline was observed under the SEM using the cryo-stage but no crystal structure could be seen.

8.6. Future Work

The characterisation and FE modelling of the wafer was performed using a single XMT scan. Further XMT scans of the wafer should be taken so as to further characterise the wafer to obtain statistically reliable information about the wafer microstructure. The data can be used to determine the cell size distribution as well as the cell wall thickness throughout the wafer. The microstructural data can be input into a Matlab script which would generate a 3D representation of the wafer. Such a script has been developed and used on a 2-dimensional level to generate a finite element mesh for composite materials. If it is extended to a 3-dimensional level, this would allow wafer models of larger dimensions to be created without the need for XMT scans. As explained previously, the resolution of the XMT image stack decreases as the sample size increases. With a computer generated model, a wafer specimen of multiple RVEs can be created at a high enough resolution to detect the thin cell walls.

The image stack from the in-situ XMT compression test which was performed in this study was partially obscured due the presence of the two compression plates. Another in-situ XMT test should be conducted, however this time an initial scan should be taken which shows the entire wafer structure. This initial image stack should then be meshed and subjected to an FE analysis. The deformation of this model could then be directly compared to the in-situ XMT scans as a verification of the accuracy of the FE model in predicting the damage of the wafer cell walls. This model would be more precise than the one used in this study since the exact wafer architecture used in the scan would also be meshed for the finite element simulation.

Digital Image Correlation (DIC) software was available and could be used with in-situ SEM videos to map the local strain distribution through a sample. However, due to the three dimensional cellular nature of the wafer the DIC software would not give accurate results. The 3D images from the different stages of the in-situ XMT compression should be analysed with volumetric DIC software. This would give the local strain distribution throughout the wafer microstructure and highlight the sites of stress localisation. The results could then be directly compared with the stress or strain contour output from the finite element analysis.

The in-situ SEM cutting experiments were only able to show the crack propagation along the surface of the wafer skins. An in-situ XMT cutting experiment would show the internal damage mechanisms of the wafer sub-surface and wafer core. The XMT scans performed in this study showed that small samples were required in order to obtain images which were of high enough resolution to show the cellular microstructure of the wafer. Therefore cutting experiments should first be performed on small samples to determine a suitable sample size which would show the crack propagation of the wafer.

The finite element model of the actual wafer architecture in this study possessed limitations which prevented the simulation of the compression into the densification region. The element deletion method meant that as the model was progressively damaged, the deleted elements represented fracture of the cell walls but also lost material mass. In reality, the wafer material does not ‘disappear’ when the cell walls fracture. Damage modelling with the extended finite element method does not delete elements but instead split elements, thus

preserving the mass of the model. XFEM was a new feature available with the latest version of Abaqus (6.9) and was not fully investigated. In future modelling work, the full potential of XFEM should be researched so that it can be implemented to simulate fracture of the wafer.

In the current model, contact interactions were applied to the surfaces of all elements using the general contact module. Thus when an element was deleted, the element below it was now exposed but possessed no contact properties. A consequence of this was that after elements deleted, the remaining elements could potentially pass through each other without interacting. In order to make the simulation more accurate, the model needed to be updated after each increment so that newly exposed surfaces of elements would possess contact interaction properties. To do this, a subroutine VUINTERACTION from the Abaqus subroutine library needs to be implemented. This is a tedious but necessary task so that modelling of the penetrative blade cutting of the wafer will produce more accurate results.

If large dimensioned wafer models can be created and the contact surfaces of elements progressively updated, then a model which mimics an actual cutting experiment can be performed.

Further experimental testing on the solid praline material is required to properly characterise its material behaviour. This needs to be done in order to develop an accurate numerical model of the praline and hence the entire wafer book.

Presently, every new wafer design at Nestlé must be manufactured at the Product Technology Centre and then subjected to testing to determine its texture, which is a costly and time consuming endeavour. A potential benefit of the finite element model is its application to product development and texture analysis of the wafer. The predicted deformation curve of the FE model could be used as a ‘measure’ of the actual wafer’s texture. If the Matlab script described above was implemented, then 3D virtual wafers of different shapes and porosities could be generated. These models could then be subjected to a finite element analysis to determine the deformation curve which would be a measure of the model’s texture. This is beneficial to Nestlé since the model would be able to predict which shapes and designs can be used to give a desired texture.

References

[1] J. Mercier. *The Temptation of Chocolate*. Belgium, Editions Racine, 2007.

[2] S.T. Beckett. *The Science of Chocolate*, 1st Edition. United Kingdom, Royal Society of Chemistry, 2004.

[3] B. Diak. Strength by Chocolate. *The International Journal of Engineering Education*. 22: 925-936, 2006.

[4] G. Tannenbaum. Chocolate: A Marvelous Natural Product of Chemistry. *Journal of Chemical Education*. 82: 1131-1135, 2004.

[5] P. Fryer, K. Pinschower. The Materials Science of Chocolate. *Materials Research Society Bulletin*. 25: 25-29, 2000.

[6] H. Tewkesbury, A.G.F. Stapley, P.J. Fryer. Modelling temperature distributions in cooling chocolate moulds. *Chemical Engineering Science*, 55: 3123-3132, 1999.

[7] H. Schenk, R. Peschar. Understanding the structure of chocolate. *Radiation Physics and Chemistry*. 71: 829-835, 2004.

[8] B.V. Pàmies. *Hydration-Induced Textural Changes In Cereal Products*. PhD Thesis, University of Nottingham, 2008.

[9] N. Traitler. *Physical and Mechanical Properties of Biopolymer Cellular Solids*. PhD Thesis, University of Cambridge, 2007.

[10] H. Fusheng, Z. Zhengang. The mechanical behavior of foamed aluminum. *Journal of Materials Science*, 34: 291–299, 1999.

[11] H. Fusheng, Z. Zhengang, G. Junchang. Compressive Deformation and Energy Absorbing Characteristic of Foamed Aluminum. *Metallurgical and Materials Transactions*, 29: 1998-2497, 1998.

[12] LJ. Gibson, M.F. Ashby. *Cellular Solids Structure and properties.* 1st ed. Oxford: Pergamon Press, 1988.

[13] E. Maire, A. Fazekas, L. Salvo, R. Dendievel, S. Youssef, P. Cloetens, J.M. Letang. X-ray tomography applied to the characterization of cellular materials: Related finite element modeling problems. *Composites Science and Technology,* 63: 2431–2443, 2003.

[14] J. Adrien, E. Maire, N. Gimenez, V. Sauvant-Moynot. Experimental study of the compression behaviour of syntactic foams by in situ X-ray tomography. *Acta Materialia*, 55: 1667–1679, 2007.

[15] K.Y.G. Mccullough, N.A. Fleck, M.F. Ashby. Uniaxial Stress-Strain Behaviour of Aluminium Alloy Foams. *Acta Mater,* 47: 2323-2330, 1999.

[16] Y. Yamada, K. Shimojima, M. Mabuchi, M. Nakamura, T. Asahina, T. Mukai, H. Kanahashi, K. Higashi. Compressive deformation behavior of Al_2O_3 foam. *Materials Science and Engineering*, A277: 213–217, 2000.

[17] N. Gupta, Kishore, E. Woldesenbet, S. Sankaran. Studies on compressive failure features in syntactic foam material. *Journal of Materials Science*, 36: 4485–4491, 2001.

[18] E. Andrews, W. Sanders, L.J. Gibson. Compressive and tensile behaviour of aluminum foams. *Materials Science and Engineering*, A270: 113–124, 1999.

[19] J. T. Beals, M. S. Thompson. Density gradient effects on aluminium foam compression behavior. *Journal of Materials Science*, 32: 3595–3600, 1997.

[20] A.H. Alaoui, T. Woignier, G.W. Scherer, J. Phalippou. Comparison between flexural and uniaxial compression tests to measure the elastic modulus of silica aerogel. *Journal of Non-Crystalline Solids*, 354: 4556–4561, 2008.

[21] M.N. Charalambides, S.M. Goh, S.L. Lim, J.G. Williams. The analysis of the frictional effect on stress - strain data from uniaxial compression of cheese. *Journal of Materials Science*. 36: 2313-2321, 2001.

[22] M.N. Charalambides, J.G. Williams, S. Chakrabarti. A study of the influence of ageing on the mechanical properties of Cheddar cheese. *Journal of Materials Science*. 30: 3959-3967, 1995.

[23] H. Luyten, J.J. Plijter, T. Van Vliet. Crispy/crunchy crusts of cellular solid foods: A literature review with discussion. *Journal of Texture Studies*. 35: 445–492, 2004.

[24] H. Luyten, T. Van Vliet. Acoustic emission, fracture behavior and Morphology of dry crispy foods: a Discussion article. *Journal of Texture Studies*. 37: 221–240, 2006.

[25] H.G. Allen. *Analysis and design of structural sandwich panels*. Oxford: Pergamon Press, 1969.

[26] K. Mohana, Y. Hona, S. Idapalapati, H.P. Seowa. Failure of sandwich beams consisting of alumina face sheet and aluminum foam core in bending. *Materials Science and Engineering*, A 409: 292–301, 2005.

[27] I.M. Daniel, J.L. Abot. Fabrication, testing and analysis of composite sandwich beams. *Composites Science and Technology*, 60: 2455-2463, 2000.

[28] C. Chen, A.M. Harte, N.A. Fleck. The plastic collapse of sandwich beams with a metallic foam core. *International Journal of Mechanical Sciences*, 43: 1483-1506, 2001.

[29] C.A. Steeves, N.A. Fleck. Collapse mechanisms of sandwich beams with composite faces and a foam core, loaded in three-point bending. Part II: experimental investigation and numerical modeling. *International Journal of Mechanical Sciences*, 46: 585–608, 2004.

[30] A. Pollien, Y. Conde, L. Pambaguian, A. Mortensen. Graded open-cell aluminium foam core sandwich beams. *Materials Science and Engineering*, 404: 9–18, 2005.

[31] T.M. McCormack, R. Miller, O. Kesler, L.J. Gibson. Failure of sandwich beams with metallic foam cores. *International Journal of Solids and Structures,* 38: 4901-4920, 2001.

[32] H. Bart-Smith, J.W. Hutchinson, A.G. Evans. Measurement and analysis of the structural performance of cellular metal sandwich construction. *International Journal of Mechanical Sciences*, 43: 1945-1963, 2001.

[33] S. Timoshenko. *Strength of Materials Part 1 Elementary. 3rd* ed. Canada: VNR, 1955.

[34] S. Timoshenko. *Strength of Materials Part 2 Advanced. 3rd* ed. Canada: VNR, 1958.

[35] F. Romano, G. Zingone. Deflections Of Beams With Varying Rectangular Cross Section. *Journal of Engineering Mechanics,* 118: 2128-2134, 1992.

[36] F. Romano. Deflections Of Timoshenko Beam With Varying Cross-Section. *lnt. J. Mech. Sci.,* 38: 1017-1035, 1996.

[37] A.G. Atkins. *The Science and Engineering of Cutting: The Mechanics and Processes of Separating, Scratching and Puncturing Biomaterials, Metals and Non-Metals*. United Kingdom, Butterworth-Heinemann, 2009.

[38] A. Dowgiallo. Cutting force of fibrous materials. *Journal of Food Engineering*. 66: 57-61, 2005.

[39] C. Gamonpilas, M.N. Charalambides, J.G. Williams. Determination of large deformation and fracture behaviour of starch gels from conventional and wire cutting experiments. *Journal of Materials Science*, 44: 4976-4986, 2009.

[40] C. Gamonpilas, M.N. Charalambides, J.G. Williams, P.J. Dooling, S.R. Gibbon. Characterisation of Fracture Behaviour of Starch Gels Using Conventional Fracture Mechanics and Wire Cutting Tests. *The XV International Congress on Rheology: The Society of Rheology 80th Annual Meeting. AIP Conference Proceedings*. 1027: 1232-1234, 2008.

[41] J.Y. Buffiere, E. Maire, J. Adrien, J.P. Masse, E. Boller. In Situ Experiments with X-ray Tomography: An Attractive Tool for Experimental Mechanics. *Experimental Mechanics*, 50: 289–305, 2010.

[42] K.S. Lim, M. Barigou. X-ray micro-computed tomography of cellular food products. *Food Research International*. 37: 1001–1012, 2004.

[43] A.M. Trater, S. Alavi, S.S.H. Rizvi. Use of Non-Invasive X-Ray Microtomography for Characterizing Microstructure of Extruded Biopolymer Foams. *Food Research International*, 38: 709–719, 2005.

[44] A. Elmoutaouakkil, L. Salvo, E. Maire, G. Peix. 2D and 3D Characterization of Metal Foams Using X-ray Tomography. *Advanced Engineering Materials*, 10: 803–807, 2002.

[45] J.R. Jones, P.D. Lee, L.L. Hench. Hierarchical porous materials for tissue engineering. *Phil. Trans. R. Soc. A,* 364: 263–281, 2006.

[46] L. Salvo, P. Cloetens, E. Maire, S. Zabler, J.J. Blandin, J.Y. Buffiere , W. Ludwig, E. Boller, D. Bellet, C. Josseron. X-ray micro-tomography an attractive characterisation technique in materials science. *Nuclear Instruments and Methods in Physics Research*, 200: 273–286, 2003.

[47] D. Chen, D. R. Chittajallu, G. Passalis, I. A. Kakadiaris. Computational Tools for Quantitative Breast Morphometry Based on 3D Scans. *Annals of Biomedical Engineering*, 38: 1703-1718, 2010.

[48] E. Maire, P. Colombob, J. Adrien, L. Babout, L. Biasetto. Characterization of the morphology of cellular ceramics by 3D image processing of X-ray tomography. *Journal of the European Ceramic Society*, 27: 1973–1981, 2007.

[49] I.G. Watson, P.D. Lee, R.J. Dashwood, P. Young. Simulation of the Mechanical Properties of an Aluminum Matrix Composite using X-Ray Microtomography. *Metallurgical and Materials Transactions*, 37A: 551-558, 2006.

[50] G. van Dalen, H. Blonk, H. van Aalst, C.L. Hendriks. 3-D Imaging of Foods Using X-Ray Microtomography. *G.I.T. Imaging & Microscopy*, 3: 18–21, 2003.

[51] M.E. Miquel, L.D. Hall. Measurement by MRI of storage changes in commercial chocolate confectionery products. *Food Research International*, 35: 993–998, 2002.

[52] Y. Tsukakoshi, S. Naito, N. Ishida. Fracture intermittency during a puncture test of cereal snacks and its relation to porous structure. *Food Research International*, 41: 909–917, 2008.

[53] J.Y. Buffière, P. Cloetens, W. Ludwig, E. Maire, L. Salvo. In Situ X-Ray Tomography Studies of Microstructural Evolution Combined with 3D Modeling. *MRS Bull*, 33: 611-619, 2008.

[54] T. Dillardy, F. N'guyen, E. Maire, L. Salvo, S. Forest, Y. Bienvenuy, J.D. Bartouty, M. Croset, R. Dendievel, P. Cloetens. 3D quantitative image analysis of open-cell nickel foams under tension and compression loading using X-ray microtomography. *Philosophical Magazine*, 85: 2147–2175, 2005.

[55] S. Youssef , E. Maire, R. Gaertner. Finite element modelling of the actual structure of cellular materials determined by X-ray tomography. *Acta Materialia*, 53: 719–730, 2005.

[56] Q. Zhang, P.D. Lee, R. Singh, G. Wua, T.C. Lindley. Micro-CT characterization of structural features and deformation behavior of fly ash/aluminum syntactic foam. *Acta Materialia*, 57: 3003–3011, 2009.

[57] S. Guessasma, P. Babin, G. Della Valle, R. Dendievel. Relating cellular structure of open solid food foams to their Young's modulus: Finite element calculation. *International Journal of Solids and Structures*, 45: 2881–2896, 2008.

[58] I. Jeon, K. Katou, T. Sonoda, T. Asahina, K. Kang. Cell wall mechanical properties of closed-cell Al foam. *Mechanics of Materials,* 41: 60–73, 2009.

[59] I. Jeon, T. Asahina, K. Kang, S. Im, T.J. Lu. Finite element simulation of the plastic collapse of closed-cell aluminum foams with X-ray computed tomography. *Mechanics of Materials*, 42: 227–236, 2010.

[60] O. Caty, E. Maire, S. Youssef, R. Bouchet. Modeling the properties of closed-cell cellular materials from tomography images using finite shell elements. *Acta Materialia,* 56: 5524–5534, 2008.

[61] S. A. Sánchez, J. Narciso, F. Rodríguez-Reinoso, D. Bernard, I. G. Watson, P. D. Lee, R. J. Dashwood. Characterization of Lightweight Graphite Based Composites Using X-Ray Microtomography. *Advanced Engineering Materials*, 8: 491-495, 2006.

[62] P.M. Falcone, A. Baiano, F. Zanini, L. Mancini, G. Tromba, D. Dreossi, F. Montanari, N. Scuor, M.A. Del Nobile. Three-dimensional Quantitative Analysis of Bread Crumb by X-ray Microtomography. *Journal of Food Science*, 70: 265-272, 2005.

[63] P. Babin, G. Della Valle, R. Dendievel, N. Lassoued, L. Salvo. Mechanical properties of bread crumbs from tomography based Finite Element simulations. *Journal of Materials Science*. 40: 5867–5873, 2005.

[64] D. Fuloria, P.D. Lee. An X-ray microtomographic and finite element modeling approach for the prediction of semi-solid deformation behaviour in Al–Cu alloys. *Acta Materialia*, 57: 5554–5562, 2009.

[65] J.G.F. Wismans, J.A.W. van Dommelen, L.E. Govaert, H.E.H. Meijer. X-ray computed tomography based modeling of polymeric foams. *Materials Science Forum*, 638-642: 2761-2765, 2010.

[66] B. Zhang, Z. Yang, X. Sun, Z. Tang, B. Zhang. A virtual experimental approach to estimate composite mechanical properties: Modeling with an explicit finite element method. *Computational Materials Science,* 49: 645-651, 2010.

[67] C. Ye-Kai, Y. Jiang-Miao, Z. Xiao-Ning. Micromechanical analysis of damage evolution in splitting test of asphalt mixtures. *Journal of Central South University of Technology*, 17: 628−634, 2010.

[68] J. Segurado, J. Llorca. A new three-dimensional interface finite element to simulate fracture in composites. *International Journal of Solids and Structures*, 41: 2977–2993, 2004.

[69] M.V. Donadon, S.F.M. de Almeida, M.A. Arbelo, A.R. de Faria. A Three-Dimensional Ply FailureModel for Composite Structures. *International Journal of Aerospace Engineering*, 2009.

[70] I. Lapczyk, J.A. Hurtado. Progressive damage modeling in fiber-reinforced materials. *Composites*, 38: 2333–2341, 2007.

[71] I.V. Ivanov, T.Sadowski. Numerical modelling and investigation of plywood progressive failure in CT tests. *Computational Materials Science*, 45: 729–734, 2009.

[72] H. Khoramishad, A.D. Crocombe, K.B. Katnam, I.A. Ashcroft. Predicting fatigue damage in adhesively bonded joints using a cohesive zone model. *International Journal of Fatigue*, 32: 1146-1158, 2010.

[73] H. Badreddine, C. Labergère, K. Saanouni, W. Rajhi, A. Rassineux, D. Kircher. F.E. elastoplastic damage model with 2D adaptive remeshing procedure for fracture prediction in metal forming simulation. *International Journal of Material Forming*, 1: 109 –112, 2008.

[74] M. Khelifa, M. Oudjene, A. Khennane. Fracture in sheet metal forming: Effect of ductile damage evolution. *Computers and Structures*, 85: 205–212, 2007.

[75] J.P. Fan, C.Y. Tang, C.P. Tsui, L.C. Chan, T.C. Lee. 3D finite element simulation of deep drawing with damage development. *International Journal of Machine Tools & Manufacture*, 46: 1035–1044, 2006.

[76] D. Steglich, W. Brocks, J. Heerens, T. Pardoen. Anisotropic ductile fracture of Al 2024 alloys. *Engineering Fracture Mechanics*, 75: 3692–3706, 2008.

[77] M. Farzin, H.R. Javani, M. Mashayekhi, R. Hambli. Analysis of blanking process using various damage criteria. *Journal of Materials Processing Technology*, 177: 287–290, 2006.

[78] H. Yu D.Y. Jeong, J.E. Gordon, Y.H. Tang. Analysis Of Impact Energy To Fracture Unnotched Charpy Specimens Made From Railroad Tank Car Steel. *Proceedings of the 2007 ASME Rail Transportation Division Fall Technical Conference*, 2007.

[79] J. Yan, J.S. Strenkowski, A finite element analysis of orthogonal rubber cutting. *Journal of Materials Processing Technology*, 174: 102–108, 2006.

[80] S.L. Sooa, D.K. Aspinwall, R.C. Dewes. 3D FE modelling of the cutting of Inconel 718. *Journal of Materials Processing Technology*, 150: 116–123, 2004.

[81] E. Ng, D.K. Aspinwall. Modelling of hard part machining. *Journal of Materials Processing Technology*, 127: 222–229, 2002.

[82] Simulai. ABAQUS User Manual, Version 6.9-1, 2009.

[83] Z. Liu; M.G. Scanlon. Modelling Indentation of Bread Crumb by Finite Element Analysis. *Biosystems Engineering*, 85: 477–484, 2003.

[84] F. Dirschmid, H. Hooputra, H.U. Mader, H. Werner. Migration of Crash Simulation Software at BMW. *ABAQUS Users' Conference,* 2005.

[85] V.S. Deshpande, N.A. Fleck. Isotropic constitutive models for metallic foams. *Journal of the Mechanics and Physics of Solids,* 48: 1253-1283, 2000.

[86] N.J. Mills, H.X. Zhu. The high strain compression of closed-cell polymer foams. *Journal of the Mechanics and Physics of Solids*. 47: 669-695, 1999.

[87] Y. Masso-Moreu, N.J. Mills. Impact compression of polystyrene foam pyramids. *International Journal of Impact Engineering*, 28: 653–676, 2003.

[88] V. Rizov, A. Shipsha, D. Zenkert. Indentation study of foam core sandwich composite panels. *Composite Structures*, 69: 95–102, 2005.

[89] C.A. Steeves, N.A. Fleck. Collapse mechanisms of sandwich beams with composite faces and a foam core, loaded in three-point bending. Part II: experimental investigation and numerical modeling. *International Journal of Mechanical Sciences*, 46: 585–608, 2004.

[90] V.I. Rizov. Non-linear indentation behavior of foam core sandwich composite materials—A 2D approach. *Computational Materials Science*, 35: 107–115, 2006.

[91] A. Korinets, H. Alehossein. Technical Note On the Initial Non-Linearity of Compressive Stress-Strain Curves for Intact Rock. *Rock Mechanics and Rock Engineering*, 35: 319-328, 2002.

[92] S. C. Warburton, A. M. Donald, A. C. Smith. The deformation of brittle starch foams. *Journal Of Materials Science*, 25: 4001-4007, 1990.

[93] ASTM: D 5934 – 02. Standard Test Method for Determination of Modulus of Elasticity for Rigid and Semi-Rigid Plastic Specimens by Controlled Rate of Loading Using Three-Point Bending.

[94] Standard Test Method for Determination of Modulus of Elasticity for Rigid and Semi-Rigid Plastic Specimens by Controlled Rate of Loading Using Three-Point Bending1 Designation: D 5934 – 02.

[95] J. Lee, M.N. Charalambides, J.G. Williams. *Mechanics of Cutting of Wafers*. Masters Project, Imperial College London, 2006.

[96] I. Kamyab, S. Chakrabarti, J.G. Williams. Cutting cheese with wire. *Journal of Materials Science*. 33: 2763-2770, 1998.

[97] A.W. Paul. Volume and density determinations for particle technologists. Micromeritics Instrument Corp., 1–16, 2001.

[98] Avizo. Visualization Sciences Group, Whyteleafe Surrey, CR3 OBL, UK.

[99] Z.L. Wang, J.C.M. Teo, C.K. Chui, S.H. Ong, C.H. Yan, S.C. Wang, H.K. Wong, S.H. Teoh. Computational biomechanical modelling of the lumbar spine using marching-cubes

surface smoothened finite element voxel meshing. *Computer Methods and Programs in Biomedicine*, 80: 25-35, 2005.

[100] M.F. Ashby, R.H. Jones. *Engineering Materials 2*. 2nd ed. Oxford: Butterworth-Heinemann Ltd., 1998.

[101] B.B. Johnsen, A.J. Kinloch, R.D. Mohammed, A.C. Taylor. Toughening mechanisms of nanoparticle-modified epoxy polymers. *Polymer*. 48: 530-541, 2007.

[102] O. Stapountzi, M.N. Charalambides, J.G. Williams. Micromechanical models for stiffness prediction of alumina trihydrate (ATH) reinforced poly (methyl methacrylate) (PMMA): Effect of filler volume fraction and temperature. *Composites Science and Technology,* 69: 2015–2023, 2009.

[103] T.D. Fornes, D.R. Paul. Modeling properties of nylon 6/clay nanocomposites using composite theories. *Polymer*, 44: 4993–5013, 2003.

[104] H. Tan, Y. Huang, C. Liu, P.H. Geubelle. The Mori–Tanaka method for composite materials with nonlinear interface debonding. *International Journal of Plasticity*, 21: 1890–1918, 2005.

[105] B. Gommers, I. Verpoest, P. Van Houtte. The Mori-Tanaka Method Applied To Textile Composite Materials, *Acta Mater*, 46: 2223-2235, 1998.

[106] N. Ramakrishnan, V. S. Arunachalam. Effective elastic moduli of porous solids. *Journal of Materials Science*, 25: 3930-3937, 1990.

[107] D.P. Mondal, N. Ramakrishnan, K.S. Suresh, S. Das. On the moduli of closed-cell aluminum foam. *Scripta Materialia*, 57: 929–932, 2007.

[108] L.F. Nielsen. Elastic Properties of Two-phase Materials. *Materials Science and Engineering*, 52: 39–62, 1982.

[109] Z. Hashin, S. Shtrikman. A Variational Approach To The Theory Of The Elastic Behaviour Of Multiphase Materials. *Journal of the Mechanics and Physics of Solids*, 11: 127-140, 1963.

[110] H.X. Zhu, J.F. Knott, N.J. Mills. Analysis of The Elastic Properties Of Open-Cell Foams With Tetrakaidecahedral Cells. *Mech. Phys. Solids,* 45: 319-343, 1997.

[111] R. M. Christensen. Mechanics Of Low Density Materials, *J. Mech. Phys. Solids,* 34: 563-578, 1986.

[112] K.K. Phani, R.N. Mukerjee. Elastic properties of porous thermosetting polymers. *Journal of Materials Science,* 22: 3453-3458, I987.

[113] Solidworks. Dassault Systèmes SolidWorks Corp, Concord, MA, USA.

[114] E. Pierres, M.C. Baietto, A. Gravouil, G. Morales-Espejel. 3D two scale X-FEM crack model with interfacial frictional contact: Application to fretting fatigue. *Tribology International*, 43: 1831-1841, 2010

[115] F.J. Harewood, P.E. McHugh. Comparison of the implicit and explicit finite element methods using crystal plasticity. *Computational Materials Science*, 39: 481–494, 2007.

[116] E.L. Keijbets, J. Chen, J. Vieira. Chocolate demoulding and effects of processing conditions. *Journal of Food Engineering*, 98: 133-140, 2009.

[117] Z.P. Bažant, Y. Xiang. Size effect in compression fracture: splitting crack band propagation. *Journal of Engineering Mechanics*, 123: 162-172, 1997.

[118] H.W. Haslach, R.W. Armstrong. *Deformable Bodies and Their Material Behaviour*. United States of America, John Wiley & Sons, Inc, 2004.

[119] J.F.V. Vincent. Application of fracture mechanics to the texture of food. *Engineering Failure Analysis*, 11: 695-704, 2004.

[120] B.J. James, B.G. Smith. Surface structure and composition of fresh and bloomed chocolate analysed using X-ray photoelectron spectroscopy, cryo-scanning eletron microscopy and environmental scanning electron microscopy. *Food Science and Technology*, 42: 929-937, 2009.

Appendix A: The material data from the square compression tests and the three point bending tests for the different sample sizes

Table A1 The compressive modulus and fracture stress of square wafer sheets of different sizes

Length of Square	2.5mm	5.0mm	7.5mm	12.5mm
Compressive Modulus (MPa)	3.87 ± 0.69	4.30 ± 0.31	4.67 ± 0.43	4.23 ± 0.58
Fracture Stress (MPa)	0.38 ± 0.08	0.43 ± 0.06	0.35 ± 0.07	0.32 ± 0.03

Table A2 The flexural stiffness of wafer beams of different sizes

Dimensions of the Wafer Beam	60 x 18 mm	80 x 10 mm	100 x 25 mm	120 x 15 mm
Stiffness (N/mm)	0.899 ± 0.034	0.182 ± 0.032	0.219 ± 0.023	0.0748 ± 0.0011

Appendix B1: Solid Volume with Gas Pycnometry

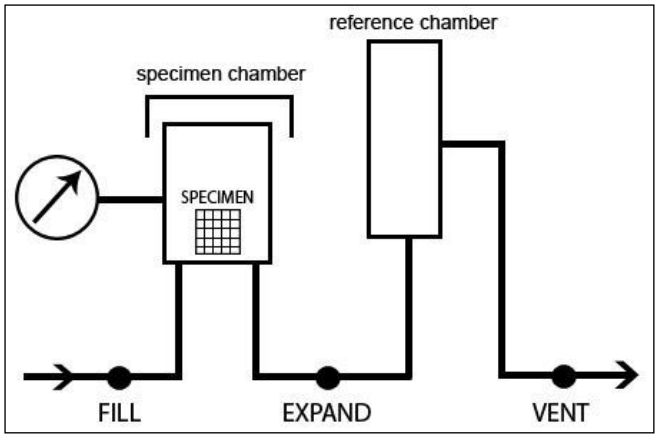

Figure B1.1 – Schematic of the helium pycnometry process

A wafer sample of unknown volume (V_x) is placed in a sealed chamber of volume (V_s) and pressure (P_s). An isolated chamber has a volume (V_r) and pressure (P_r). The gas law is applied to this initial system in Equation B1.1.

$$P_s(V_s - V_x) + P_r V_r = nRT \qquad \text{(B1.1)}$$

After the valve is opened the pressure equilibrates in both chambers to (P_{sys}). The gas law is applied to the equilibrated system in Equation B1.2.

$$P_{sys}(V_s + V_r - V_x) = nRT \tag{B1.2}$$

By equating Equation B1.1 and Equation B1.2 , the volume of the wafer can be found.

$$P_s(V_s - V_x) + P_r V_r = P_{sys}(V_s + V_r - V_x) \tag{B1.3}$$

Equation B1.3 is then rearranged in order to find an expression for the volume of the wafer sample.

$$V_x = \frac{P_{sys}V_s + P_{sys}V_r - P_s V_s - P_r V_r}{P_{sys} - P_s} \tag{B1.4}$$

Where *n*, *R* and *T* are constants from the gas law

Appendix B2: Bulk Density with Glass Beads

The total mass (m_t) is the sum of the mass of the beads (m_b) and the mass of the wafer (m_w) as expressed in Equation B2.1.

$$m_b = m_t - m_w \tag{B2.1}$$

Since the mass and density (ρ_b) of the beads are known, its volume (V_b) can be found from Equation B2.2.

$$V_b = \frac{m_b}{\rho_b} \tag{B2.2}$$

The volume of the wafer (V_w) can be expressed In Equation B2.3 as the ratio of its mass to density (ρ_w) or the difference between the total volume (V_t) and the volume of the beads (V_b).

$$V_w = \frac{m_w}{\rho_w} = V_t - V_b \tag{B2.3}$$

By substituting Equation B2.1 and Equation B2.2 into the V_b term of Equation B2.3, the wafer density ρ_w can be expressed as Equation B2.4.

$$\rho_w = \frac{m_w}{V_t - \frac{(m_t - m_w)}{\rho_b}} \qquad \text{(B2.4)}$$

Appendix C1

Wafer Skin Transformation in Bending for Sandwich Analysis 1

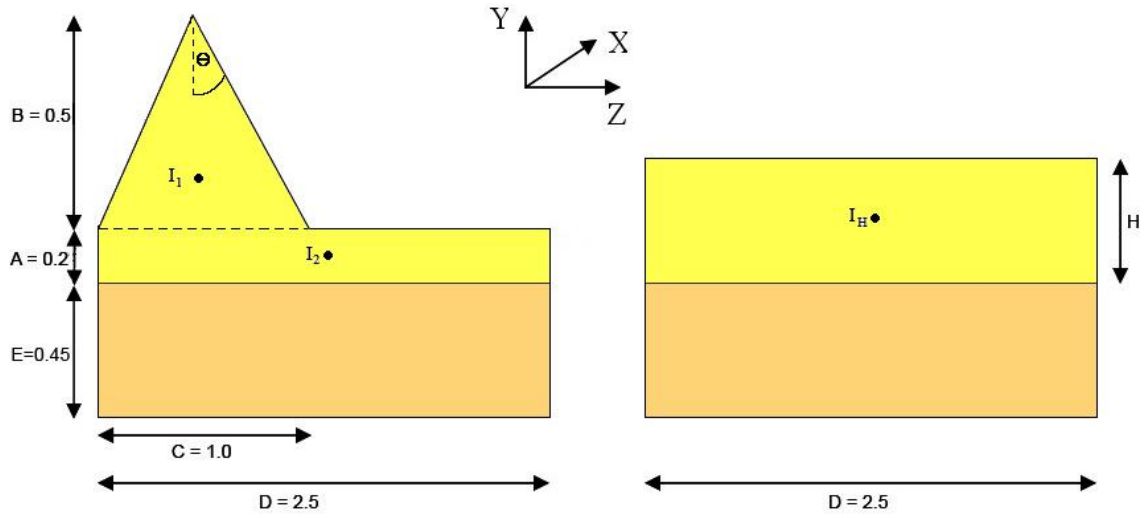

Figure C1.1 Cross-sectional face of an element of the actual wafer and the equivalent wafer

The skin can be separated into two sections, labelled 1 and 2 in Figure C1.1, for the analysis of its 2nd Moment of Area. The 2nd moment of area of section 1 (I_1) about its centroid is given in Equation C1.1.

$$I_1 = \frac{CB^3}{36} \qquad \text{(C1.1)}$$

The geometric centre of the wafer sheet is considered as the neutral axis. The 2nd moment of area of section 1 about the neutral axis (I_{1O}) is found by the parallel axis theorem and given by Equation C1.2.

$$I_{1O} = \frac{CB^3}{36} + \frac{CB}{2}\left(E + A + \frac{B}{3}\right)^2 \qquad \text{(C1.2)}$$

The 2nd moment of area of section 2 (I_2) is given by Equation C1.3.

$$I_2 = \frac{DA^3}{12} \tag{C1.3}$$

The 2nd moment of area of the section 2 about the neutral axis (I_{2O}) is found using the parallel axis theorem and given by Equation C1.4.

$$I_{2O} = \frac{DA^3}{12} + DA\left(E + \frac{A}{2}\right)^2 \tag{C1.4}$$

The total 2nd moment of area of the wafer skin (I_{TOTAL}) about the neutral axis is found by the sum of Equation C1.2 and Equation C1.4.

$$I_{TOTAL} = I_{1O} + I_{2O} = \frac{CB^3}{36} + \frac{CB}{2}\left(E + A + \frac{B}{3}\right)^2 + \frac{DA^3}{12} + DA\left(E + \frac{A}{2}\right)^2 \tag{C1.5}$$

The 2nd moment of area of the equivalent wafer skin (I_H) is expressed using Equation C1.6.

$$I_H = \frac{DH^3}{12} \tag{C1.6}$$

Parallel axis theorem is then applied to find the 2nd moment of area of the equivalent skin about the neutral axis (I_{H0}) as shown in Equation C1.7.

$$I_{HO} = \frac{DH^3}{12} + DH\left(E + \frac{H}{2}\right)^2 \tag{C1.7}$$

Equation C1.5 and Equation C1.7 are equated to calculate the thickness of the equivalent wafer skin (H) resulting in Equation C1.8.

$$\frac{H^3}{3} + H^2E + HE^2 = \frac{CB^3}{36D} + \frac{CB}{2D}\left(E + A + \frac{B}{3}\right)^2 + \frac{A^3}{12} + A\left(E + \frac{A}{2}\right)^2 \tag{C1.8}$$

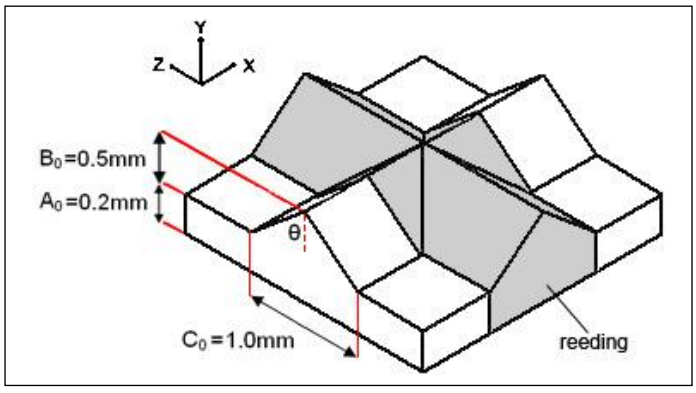

Figure C1.2 A RVE unit of the wafer skin

At different points along the x-axis of the wafer skin in Figure C1.2, the shape of the cross-section changes. This is more easily visualised in Figure C1.3.

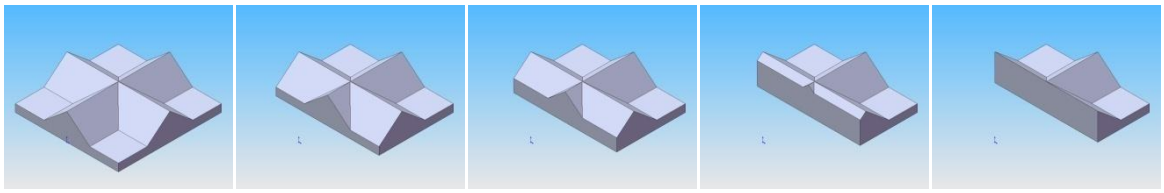

Figure C1.3 A RVE unit of the wafer skin showing how the cross-section varies along the x-axis through the reeding

Due to the variable cross-section, the constants A, B and C also vary along the axis and must be accounted for in Equation C1.8. For values of x along the increasing slope of the reeding (x = 0mm to 0.5mm), A, B and C are expressed by Equations C1.9, C1.10 and C1.11 respectively.

$$A = A_0 + \frac{B_0}{\frac{1}{2}C_0}x \qquad \text{(C1.9)}$$

$$B = (A_0 - A) + B_0 \qquad \text{(C1.10)}$$

$$C = 2B\tan\theta \qquad \text{(C1.11)}$$

Where: A_0 is the value of A at the flat section of the wafer (=0.2mm)

B_0 is the value of B at the flat section of the wafer (=0.5mm)

C_0 is the value of C at the flat section of the wafer (=1.0mm)

For values of x along the decreasing slope of the reeding (x = 0.5mm to 1.0mm), the values of A, B and C are mirrored about the values calculated for the range of x between 0mm and 0.5mm. As a result, the equivalent thickness of the skin (H) could be easily calculated at any point along the wafer in the x-axis.

Appendix C2: Wafer Core Transformation in Bending

The standard bending moment relation is expressed in Equation C2.1.

$$\frac{M}{I} = \frac{E}{R} \qquad \text{(C2.1)}$$

The 2nd Moment of Area of a rectangular cross-section is given in Equation C2.2 in terms of its width (b) and thickness (d).

$$I = \frac{bd^3}{12} \qquad \text{(C2.2)}$$

By substituting Equation C2.2 into the bending moment Equation C2.1, the bending moment can be expressed as shown in Equation C2.3.

$$\frac{M}{\frac{bd^3}{12}} = \frac{E_c}{R} \qquad \text{(C2.3)}$$

However, Equation C2.3 can be modified by decreasing the width (b_{core}) and simultaneously increasing the modulus (E_s). Thus Equation C2.3 becomes Equation C2.4.

$$\frac{M}{\frac{b_{core}d^3}{12}} = \frac{E_s}{R} \qquad \text{(C2.4)}$$

The bending moment and the radius of curvature were the same in both Equation C2.3 and Equation C2.4. and thus can be equated to each other in Equation C2.5.

$$MR = E_c \frac{bd^3}{12} = E_s \frac{b_{core}d^3}{12} \qquad \text{(C2.5)}$$

As a result, Equation C2.5 can be reduced to an expression (Equation C2.6) for the equivalent width (b_{core}) in terms of the original width (b) and both the moduli (E_c and E_s).

$$b_{core} = \frac{bE_c}{E_s} \qquad \text{(C2.6)}$$

Appendix C3: Bending Deflection Calculation

According to Timoshenko's Area-Moment Method, the deflection δ of a beam is the area under bending moment diagram (Figure C3.1) multiplied by the x-coordinate of the centroid of area, divided by the product of the 2nd moment of area and the modulus.

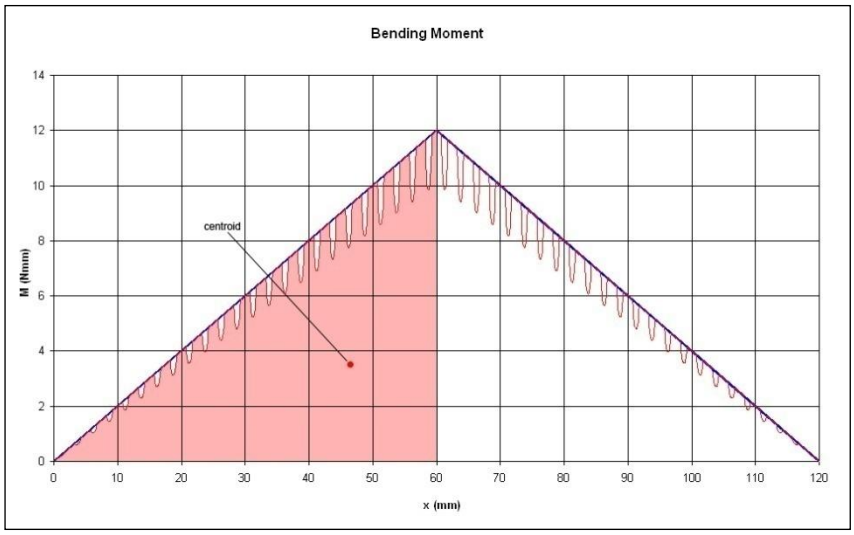

Figure C3.1 The modified (red) and uniform (blue) cross-section bending moment diagram

Mathematically the bending deflection is expressed in Equation C3.1

$$\delta = \frac{1}{EI}\int_{A}^{B} f(x).dx \left(\frac{\int_{A}^{B} x f(x).dx}{\int_{A}^{B} f(x).dx} \right) \qquad \text{(C3.1)}$$

Where $f(x)$ is the bending moment *M.*

The x-coordinate of the centroid is given in Equation C3.2.

$$\left(\frac{\int_{A}^{B} x f(x).dx}{\int_{A}^{B} f(x).dx} \right) \qquad \text{(C3.2)}$$

Equation C3.1 can then be simplified to the expression in Equation C3.3.

$$\delta = \frac{1}{EI}\int_{A}^{B} x f(x).dx \qquad \text{(C3.3)}$$

By then substituting the bending moment (M) into Equation C3.3, the bending deflection can be expressed in the form shown in Equation C3.4.

$$\delta = \int_{A}^{B} \frac{1}{EI} Mx.dx \qquad \text{(C3.4)}$$

According to Timoshenko's theory for beams of variable cross-section, the deflection of the beam can be reduced to that of constant cross-section. This is accomplished by multiplying the bending moment by the expression in Equation C3.5.

$$\frac{MI_0}{I} \tag{C3.5}$$

Where I is the 2nd moment of area of the variable cross-section beam, I0 is the 2nd moment of area of the uniform cross-section beam and $M_{uniform}$ is the 2nd moment of area of the uniform cross-section beam.

By using Equation C3.5 in Equation C3.4, the central deflection of the I-beam can be determined between the limits of 0 and L/2, using the uniform bending moment and the elastic modulus of the skin. This central deflection is expressed in Equation C3.6.

$$\delta_{central} = \frac{1}{E_{skin} I_0} \int_0^{L/2} \frac{I_0}{I} M_{uniform} x.dx \tag{C3.6}$$

This is further simplified to the integrand in Equation C3.7 with a uniform bending moment and the 2nd moment of area of the I-beam which is function of the length of the beam *x.*

$$\delta_{central} = \frac{1}{E_{skin}} \int_0^{L/2} \frac{M_{uniform}}{I} x.dx \tag{C3.7}$$

The uniform bending moment expressed in terms of the load *P* is Equation C3.8, which is then substituted into Equation C3.7.

$$M_{uniform} = \frac{Px}{2} \tag{C3.8}$$

By applying Timoshenko's theory of symmetrical beams of two different materials (Appendix C2), the core width can be represented as an equivalent width of the same modulus as the skin, thus resulting in an I-beam of a single modulus. This I-beam is shown in Figure C3.2.

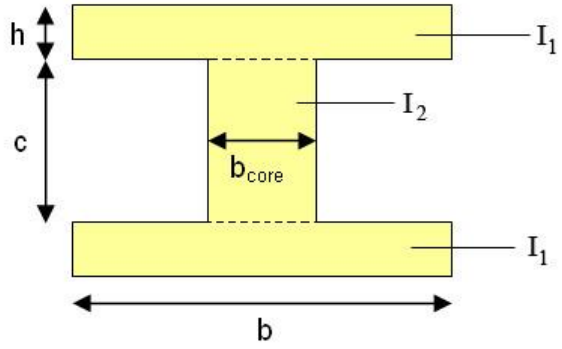

Figure C3.2 The I-beam cross-section of the equivalent wafer sheet

The 2nd moment of area of the core region can be expressed and simplied to Equation C3.9.

$$I_2 = \frac{b_{core}c^3}{12} = \frac{bc^3}{12}\left(\frac{E_{core}}{E_{skin}}\right) \qquad \text{(C3.9)}$$

The total 2nd moment of area of the beam (I) is the sum of the core (I2) and each of the two skins (I1) and is stated in Equation C3.10.

$$I = 2I_1 + I_2 \qquad \text{(C3.10)}$$

The 2nd moment of area of the skin is calculated with respect to the centre of the core as the neutral axis and is expressed in Equation C3.11.

$$I_1 = \frac{bh^3}{12} + bh\left(\frac{c}{2} + \frac{h}{2}\right)^2 \qquad \text{(C3.11)}$$

The thickness of the skin (h) is a function of x due the variable linear thickness of the reedings.

After combining Equation C3.9 and Equation C3.11 into Equation C3.10, the resulting expression for I is then substituted into Equation C3.7. The central deflection of the beam can be calculated from the integral in Equation C3.12.

$$\delta_{central} = \frac{1}{E_{skin}} \int_0^{L/2} \frac{\frac{Px^2}{2}}{\left\{2\left[\frac{bh^3}{12} + bh\left(\frac{c}{2} + \frac{h}{2}\right)^2\right] + \left[\frac{bc^3}{12}\left(\frac{E_{core}}{E_{skin}}\right)\right]\right\}} .dx \qquad \text{(C3.12)}$$

Appendix C4: Wafer in Compression

The total strain in Equation C4.1 is given by the ratio of the total displacement to the original height.

$$\varepsilon_{total} = \frac{\delta_{total}}{h} \tag{C4.1}$$

The individual strain of core and skin is given in Equation C4.2 and Equation C4.3 respectively, and calculated by the ratio of the displacement of each section to the original height of the corresponding section.

$$\varepsilon_c = \frac{\delta_c}{h_c} \tag{C4.2}$$

$$\varepsilon_s = \frac{\delta_s}{h_s} \tag{C4.3}$$

The total deflection in Equation C4.4 is given by the sum of the contributions of the individual deflections.

$$\delta_{total} = \delta_c + \delta_s \tag{C4.4}$$

Substituting the deflections in Equation C4.4 in terms of strain and height, the total strain can be expressed using the individual strains as shown in Equation C4.5.

$$\varepsilon_{total} h = \varepsilon_c h_c + \varepsilon_s h_s \tag{C4.5}$$

Equation C4.5 can be rearranged to Equation C4.6.

$$\varepsilon_{total} = \varepsilon_c \frac{h_c}{h} + \varepsilon_s \frac{h_s}{h} \tag{C4.6}$$

Assuming that the stress applied to the composite is the same in the core and the skin results in Equation C4.7.

$$\sigma = E_{compression} \varepsilon_{total} = E_s \varepsilon_s = E_c \varepsilon_c \tag{C4.7}$$

The total strain in the Equation C4.6 can be substituted into equation C4.7 resulting in Equation C4.8.

$$E_s \varepsilon_s = \left(\varepsilon_c \frac{h_c}{h} + \varepsilon_s \frac{h_s}{h} \right) E_{compression} \tag{C4.8}$$

The volume fraction (V_f) of the skin phase is expressed in Equation C4.9

$$V_f = \frac{h_s}{h} \qquad \text{(C4.9)}$$

This allows Equation C4.8 to be reduced to the form in Equation C4.10.

$$E_s = \left(\frac{\varepsilon_c}{\varepsilon_s}\left(1 - V_f\right) + V_f \right) E_{compression} \qquad \text{(C4.10)}$$

But from Equation C4.7, $\varepsilon_c E_c = \varepsilon_s E_s$, and thus Equation C4.10 can be reduced and rearranged to Equation C4.9 which expresses the equivalent elastic compressive modulus of the composite in terms of the skin and core moduli and the volume fraction of the skin.

$$E_{compression} = \frac{1}{\frac{V_f}{E_s} + \frac{1 - V_f}{E_c}} \qquad \text{(C4.11)}$$

Appendix C5: Wafer Skin and Wafer Core Transformation in Bending for Sandwich Analysis 2

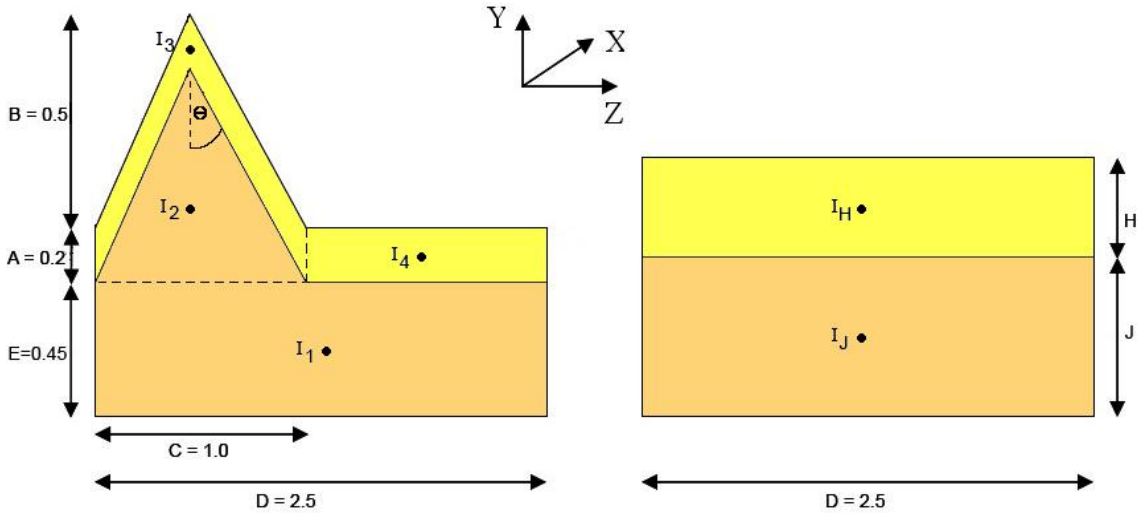

Figure C5.1 Cross-sectional face of an element of the actual wafer and the equivalent wafer

The Wafer Core Transformation

The wafer core can be separated into two sections, labelled 1 and 2 in Figure C5.1, for the analysis of its 2nd Moment of Area. The 2nd moment of area of section 1 (I_1) about its centroid is given in Equation C1.1.

$$I_1 = \frac{DE^3}{12} \tag{C5.1}$$

The geometric centre of the wafer sheet is considered as the neutral axis. The 2nd moment of area of section 1 about the neutral axis (I_{10}) is found by the parallel axis theorem and given by Equation C5.2.

$$I_{1O} = \frac{DE^3}{12} + DE\left(\frac{E}{2}\right)^2 \tag{C5.2}$$

The 2nd moment of area of section 2 (I_2) is given by Equation C5.3.

$$I_2 = \frac{CB^3}{36} \tag{C5.3}$$

The 2nd moment of area of the section 2 about the neutral axis (I_{2O}) is found using the parallel axis theorem and given by Equation C5.4.

$$I_{2O} = \frac{CB^3}{36} + \frac{CB}{2}\left(E + \frac{B}{3}\right)^2 \tag{C5.4}$$

The total 2nd moment of area of the wafer core (I_{CORE}) about the neutral axis is found by the sum of Equation C5.2 and Equation C5.4.

$$I_{TOTAL} = I_{1O} + I_{2O} = \frac{DE^3}{12} + DE\left(\frac{E}{2}\right)^2 + \frac{CB^3}{36} + \frac{CB}{2}\left(E + \frac{B}{3}\right)^2 \tag{C5.5}$$

The 2nd moment of area of the equivalent wafer core (I_J) is expressed using Equation C5.6.

$$I_J = \frac{DJ^3}{12} \tag{C5.6}$$

Parallel axis theorem is then applied to find the 2nd moment of area of the equivalent core about the neutral axis (I_{J0}) as shown in Equation C5.7.

$$I_{JO} = \frac{DJ^3}{12} + DJ\left(\frac{J}{2}\right)^2 \tag{C5.7}$$

Equation C1.5 and Equation C1.7 are equated to calculate the thickness of the equivalent wafer skin (J) resulting in Equation C5.8.

$$J^3 = E^3 + \frac{CB}{4D}\left[\frac{B^2}{3} + 6\left(E + \frac{B}{3}\right)^2\right] \quad \text{(C5.8)}$$

The Wafer Skin Transformation

The wafer skin can be separated into two sections, labelled 3 and 4 in Figure C5.1, for the analysis of its 2nd Moment of Area. The 2nd moment of area of section 3 (I_3) about its centroid is given in Equation C1.9.

$$I_3 = \frac{CB^3}{36} + \frac{CA^3}{12} - \frac{CB^3}{36} \quad \text{(C5.9)}$$

The geometric centre of the wafer sheet is considered as the neutral axis. The 2nd moment of area of section 3 about the neutral axis (I_{30}) is found by the parallel axis theorem and given by Equation C1.10.

$$I_{3O} = \left(\frac{CB^3}{36} + \frac{CB}{2}\left(A + E + \frac{B}{3}\right)^2\right) + \left(\frac{CA^3}{12} + CA\left(\frac{A}{2} + E\right)^2\right) - \left(\frac{CB^3}{36} + \frac{CB}{2}\left(\frac{B}{3} + E\right)^2\right) \quad \text{(C5.10)}$$

Equation C5.10 can then be simplified to the expression in Equation C5.11.

$$I_{3O} = \frac{CA^3}{12} + CA\left(\frac{A}{2} + E\right)^2 + \frac{CB}{2}\left(A^2 + 2AE + \frac{2AB}{3}\right) \quad \text{(C5.11)}$$

The 2nd moment of area of section 4 (I_4) is given by Equation C5.12.

$$I_4 = (D - C)\frac{A^3}{12} \quad \text{(C5.12)}$$

The 2nd moment of area of the section 4 about the neutral axis (I_{4O}) is found using the parallel axis theorem and given by Equation C5.13.

$$I_{4O} = (D - C)\frac{A^3}{12} + A(D - C)\left(E + \frac{A}{2}\right)^2 \quad \text{(C5.13)}$$

The total 2nd moment of area of the wafer skin (I_{SKIN}) about the neutral axis is found by the sum of Equation C1.2 and Equation C1.4.

$$I_{SKIN} = I_{3O} + I_{4O} = A\left[\frac{DA^2}{3} + D\left(E^2 + EA\right) + \frac{CB}{2}\left(A + 2E + \frac{2B}{3}\right)\right] \quad \text{(C5.14)}$$

The 2nd moment of area of the equivalent wafer skin (I_H) is expressed using Equation C5.15.

$$I_H = \frac{DH^3}{12} \tag{C5.15}$$

Parallel axis theorem is then applied to find the 2nd moment of area of the equivalent skin about the neutral axis (I_{H0}) as shown in Equation C5.16.

$$I_{HO} = \frac{DH^3}{12} + DH\left(J + \frac{H}{2}\right)^2 \tag{C5.16}$$

Equation C5.14 and Equation C5.16 are equated to calculate the thickness of the equivalent wafer skin (H) resulting in Equation C5.17.

$$\frac{H^3}{3} + H^2 J + HJ^2 = A\left[\frac{A^2}{3} + \left(E^2 + EA\right) + \frac{CB}{2D}\left(A + 2E + \frac{2B}{3}\right)\right] \tag{C5.17}$$

As was done in the Sandwich Analysis 1, the variation in thickness of both the skin and core along the x-axis are accounted for using Equations C1.9, C1.10 and C1.11.

Appendix D: Analytical Predictions for the Solid Modulus of Wafer

Table D1 The solid modulus values calculated for the wafer using various analytical models

Analytical Model	Solid Modulus – Entire Wafer (MPa)	Solid Modulus – Wafer Core (MPa)
Gibson & Ashby (Open)	61.5	199.9
Gibson & Ashby (Closed)	16.3	29.4
Halpin-Tsai	16.3	29.4
Ramakrishan & Arunachal	111.3	387.5
Nielsen	61.7	200.7
Hashin-Shtrikman	28.3	739.8
Chen & Lake	27.6	52.6
Christensen	32.7	58.9
Mackenzie	49.2	131.3

Appendix E: Input file of the Finite Element RVE model

For simplicity, only the first 3 nodes and last 3 nodes with corresponding coordinates of the mesh are listed. Only the first 3 elements and last 3 elements with corresponding node coordinates of the mesh are listed.

```
*Heading
** Job name: ter-E150-YS25-t20 Model name: ter15-483
** Generated by: Abaqus/CAE 6.9-1
*Preprint, echo=NO, model=NO, history=NO, contact=NO
**
** PARTS
**
*Part, name=PART-1-1
*Node
      1,  0.110232495,    0.0561595, 0.00756449997
      2, 0.0366889015, 0.0877265036, 0.00756545039
      3,  0.101343006,  0.107411005, 0.00751450006
……..
  60996,   1.93139505,   1.45720506,  0.212560505
  60997,   1.46681011,   1.64459002,       1.99482
  60998,   0.45175001,   1.86072993,  0.123117998
*Element, type=C3D4
     1, 16824, 16833, 18063, 18033
     2, 17411, 18063, 18033, 16824
     3, 22151, 21463, 21474, 21469
……..
230284, 12160, 12159, 13272, 12193
230285, 23292, 21950, 51475, 22611
230286, 12814, 11757, 13408, 59864
*Nset, nset=_PICKEDSET2, internal, generate
     1,  60998,      1
*Elset, elset=_PICKEDSET2, internal, generate
      1,  230286,       1
```

```
** Section: Section-1-_PICKEDSET2
*Solid Section, elset=_PICKEDSET2, controls=EC-1, material=MATERIAL-1
1.,
*End Part
**
*Part, name=Part-2
*End Part
**
*Part, name=Part-3
*End Part
**
**
** ASSEMBLY
**
*Assembly, name=Assembly
**
*Instance, name=PART-1-1, part=PART-1-1
*End Instance
**
*Instance, name=Part-2-1, part=Part-2
0.00333499999999998, 0.0297549999999987,    -0.069565
*Node
      1, -0.075000003,   2.28500009,   2.45000005
      2, -0.075000003,   2.30999994,   2.45000005
      3, -0.075000003,   2.30999994,           0.
……
   5098,  0.075000003,   2.28500009, 0.0500000007
   5099, 0.0250000004,   2.28500009, 0.0500000007
   5100, -0.0250000004,   2.28500009, 0.0500000007
*Element, type=R3D4
 1,   1,   2,   9, 104
 2, 104,   9,  10, 103
 3, 103,  10,  11, 102
```

```
……..
5096, 350, 349, 249, 248
5097, 349, 348, 250, 249
5098, 348,   4,   3, 250
*Node
   5101,   1.17833495,    2.2974999,   1.22500002
*Nset, nset=Part-2-1-RefPt_, internal
5101,
*Elset, elset=Part-2-1, generate
    1,  5098,     1
*End Instance
**
*Instance, name=Part-3-1, part=Part-3
     0.04247, -0.0296339999999994, -0.0709549999999995
*Node
      1,   2.42499995, 0.0270000007,   2.45000005
      2,   2.42499995, 0.00200000009,   2.45000005
      3,   2.42499995, 0.00200000009,           0.
……..
   5098,    2.2750001, 0.0270000007, 0.0500000007
   5099,   2.32500005, 0.0270000007, 0.0500000007
   5100,        2.375, 0.0270000007, 0.0500000007
*Element, type=R3D4
 1,   1,   2,   9, 104
 2, 104,   9,  10, 103
 3, 103,  10,  11, 102
……..
5096, 350, 349, 249, 248
5097, 349, 348, 250, 249
5098, 348,   4,   3, 250
*Node
   5101,   1.17499995, 0.0144999996,   1.22500002
*Nset, nset=Part-3-1-RefPt_, internal
```

```
5101,
*Elset, elset=Part-3-1, generate
    1,  5098,     1
*End Instance
**
*Nset, nset=_PickedSet36, internal, instance=Part-3-1
 5101,
*Nset, nset=_PickedSet37, internal, instance=Part-2-1
 5101,
*Nset, nset=_PickedSet25, internal, instance=PART-1-1
 47286, 47296, 47348, 47795, 47816, 47817, 47844, 47853, 47858, 47869,
……
49375, 49376, 49377, 49378, 49379, 49380, 49381
*Nset, nset=_PickedSet26, internal, instance=PART-1-1
    1,    2,    3,    4,    5,    6,    7,    8,    9,   10,   11,   12,
……..
1547, 1555, 1595
*Nset, nset=_PickedSet27, internal, instance=PART-1-1
     9,    29,   817,   818,   821,   835,  1195,  1289,  1291,  1302,
…….
48320, 48557, 48632, 48738, 48785
*Nset, nset=_PickedSet28, internal, instance=PART-1-1
   834,   838,   845,  1296,  1299,  1300,  1301,  1310,  1712,  1724,
……..
47790, 47793, 47797, 47811, 48299, 48669, 48674, 48703, 48724, 48730
*Rigid Body, ref node=Part-2-1.Part-2-1-RefPt_, elset=Part-2-1.Part-2-1
*Rigid Body, ref node=Part-3-1.Part-3-1-RefPt_, elset=Part-3-1.Part-3-1
*End Assembly
**
** ELEMENT CONTROLS
**
*Section Controls, name=EC-1, ELEMENT DELETION=YES
1., 1., 1.
*Amplitude, name=Amp-1
         0.,          0.,          10.,          1.
```

```
*Amplitude, name=Amp-2, definition=SMOOTH STEP
          0.,           0.,          20.,           1.
**
** MATERIALS
**
*Material, name=MATERIAL-1
*Damage Initiation, criterion=DUCTILE
 0.001,0.,0.
*Damage Evolution, type=ENERGY
0.,
*Density
1.,
*Elastic
150.,0.
*Plastic
25.,0.
**
** INTERACTION PROPERTIES
**
*Surface Interaction, name=IntProp-1
**
** INTERACTIONS
**
** Interaction: Int-1
*Contact, op=NEW
*Contact Inclusions, ALL EXTERIOR
*Contact property assignment
 ,  , IntProp-1
** ----------------------------------------------------------------
**
** STEP: Step-1
**
*Step, name=Step-1
```

```
*Dynamic, Explicit
, 20.
*Bulk Viscosity
0.06, 1.2
** Mass Scaling: Reinitialize Mass
**               Whole Model
*Fixed Mass Scaling
**
** BOUNDARY CONDITIONS
**
** Name: BC-1 Type: Displacement/Rotation
*Boundary, amplitude=Amp-2
_PickedSet36, 1, 1
_PickedSet36, 2, 2, 0.25
_PickedSet36, 3, 3
_PickedSet36, 4, 4
_PickedSet36, 5, 5
_PickedSet36, 6, 6
** Name: BC-2 Type: Displacement/Rotation
*Boundary, amplitude=Amp-2
_PickedSet37, 1, 1
_PickedSet37, 2, 2, -0.25
_PickedSet37, 3, 3
_PickedSet37, 4, 4
_PickedSet37, 5, 5
_PickedSet37, 6, 6
** Name: BC-3 Type: Symmetry/Antisymmetry/Encastre
*Boundary
_PickedSet25, ZSYMM
** Name: BC-4 Type: Symmetry/Antisymmetry/Encastre
*Boundary
_PickedSet26, ZSYMM
** Name: BC-5 Type: Symmetry/Antisymmetry/Encastre
```

```
*Boundary
_PickedSet27, XSYMM
** Name: BC-6 Type: Symmetry/Antisymmetry/Encastre
*Boundary
_PickedSet28, XSYMM
**
** OUTPUT REQUESTS
**
*Restart, write, number interval=1, time marks=NO
**
** FIELD OUTPUT: F-Output-1
**
*Output, field, number interval=50
*Node Output
CF, RF, U
*Element Output, directions=YES
LE, PE, PEEQ, PEMAG, S, SDEG, STATUS
*Contact Output
CSTRESS,
**
** HISTORY OUTPUT: H-Output-1
**
*Output, history, variable=PRESELECT, frequency=1
*End Step
```